26

IS-T-1838

Microstructure-strength Relationship of a Deformation Processed Aluminum-titanium Composite

by

Lund, Tone

MS Thesis submitted to Iowa State University

Ames Laboratory, U.S. DOE
Iowa State University
Ames, Iowa 50011

Date Transmitted: February 23, 1998

PREPARED FOR THE U.S. DEPARTMENT OF ENERGY
UNDER CONTRACT NO. W-7405-Eng-82.

DISCLAIMER

This report has been reproduced directly from the best available copy.

AVAILABILITY:

To DOE and DOE contractors: Office of Scientific and Technical Information
P.O. Box 62
Oak Ridge, TN 37831

prices available from: (615) 576-8401
FTS: 626-8401

To the public: National Technical Information Service
U.S. Department of Commerce
5285 Port Royal Road
Springfield, VA 22161

DISCLAIMER

Portions of this document may be illegible electronic image products. Images are produced from the best available original document.

Microstructure-strength relationship of a deformation processed aluminum-titanium composite

Tone Lund

Major Professor: L. Scott Chumbley

Iowa State university

The mechanical properties, electrical properties and microstructures have been evaluated for an Al-20 wt % Ti deformation processed metal metal matrix composite (DMMC). The strength of the swaged, extruded and wire drawn composite increases several-fold with increasing deformation up to a true strain of 12.1, the maximum investigated. At this point the Ti was elongated and SEM and TEM analysis of the transverse direction of the wire showed the ribbon-like filaments that are common for this type of material. Texture development was also characterized to explain the deformation characteristics of the composite materials. The Ti filaments acquired a $\langle 10\bar{1}0 \rangle$ fiber texture during deformation, and the Al filaments acquired a dual texture of (111) and (100). Resistivity measurements of the composite showed that for the highest deformed sample ($\eta = 12.1$), the resistivity increased linearly with temperature up to the temperature where Al_3Ti formed. At this point the slope increased. Beyond this point, the resistivity of the sample never returned to its original value. The temperature where Al_3Ti forms was investigated using DTA and XRD analysis. The reaction temperature decreases with increasing deformation true strain (η) and filament spacing.

TABLE OF CONTENTS

1 DEFORMATION PROCESSED COMPOSITES

1.1 General introduction

Previous studies of deformation processed metal metal matrix composites (DMMC's) have shown anomalous strengthening in FCC matrix materials such as Cu [1-10] and Al [11, 12] containing BCC second phase metals (e.g. Nb, Fe, or Cr). More recent studies of Ti-20Y [13-16], Mg-20X (where X = Fe, Nb, and Ti), and Mg-8Li/5Ti [17-19] have demonstrated the potential for hexagonal close packed (HCP) phases to benefit similarly from deformation processing and have shown that texture development in the matrix and fiber phases has a significant influence on the processing and properties of the composite material. The work done on HCP composites indicates that axisymmetrically deformed HCP metals in DMMC's develop a $\langle 10\bar{1}0 \rangle$ fiber texture. This texture restricts the HCP phase to plane strain. These results suggest that an FCC matrix containing an HCP second phase might also display anomalous strengthening if deformation processed. In this study an FCC Al matrix containing an HCP Ti reinforcing phase was deformation processed to a true strain of 12.1 to determine whether anomalous strengthening would be produced and, if so, whether a useful engineering material might result.

1.2 Cu-X composites

During the past several years, Cu-based DMMC materials have been developed with extraordinary mechanical and electrical properties [2-10]. These alloys, comprised of Cu (FCC) with 10 to 30 vol% of Nb, Ta, Cr, V or Fe, are heavily deformed to produce nanometer-scale filaments of the secondary phase embedded in the Cu matrix. The Cu-20Nb system is the most thoroughly studied of these alloys and has ultimate tensile strengths (UTS) in excess of 2200 MPa after deformation to a true strain of $\eta = 12$ [6], where $\eta = \ln (A_0/A)$ and A_0 and A are the initial and final cross-sectional areas, respectively. For sheet materials, an effective deformation strain used for comparison to true deformation rod materials is calculated as $\eta_e=(2/\sqrt{3})\eta$ [20], assuming negligible lateral spread, which corresponds to $\eta_e=(2/\sqrt{3})\ln(t/t_0)$, where t_0 and t are the initial and final thicknesses of the sheet, respectively.

The Cu-X alloys are characterized by remarkable ductility, which allows cast or powder-processed starting billets to be drawn to strains as high as η =13.4 (99.99985%

reduction in area) before breaking [9]. Such deformations represent more than an 800-fold reduction in diameter and are accompanied by a corresponding reduction in the size and spacing of the second phase. Thus, an as-cast billet of Cu-20Nb, displaying Nb dendrites with an average thickness of 5μm, may be deformation processed at room temperature into a composite wire containing Nb filaments with an average thickness of 7 nm [10]. Such composites formed *in-situ* have tensile strengths much higher than those of any other Cu alloys and higher than the strengths predicted from the rule-of-mixtures (ROM) calculations [21]. Figure 1 shows the UTS data for Cu, Nb, and Cu-20Nb, as well as the ROM strength predictions for such a composite. Debate continues on the mechanism(s) which account for the high strengths of the Cu-X alloys, but discussion centers on the role of the nanoscale filamentary structure in impeding the generation and propagation of dislocations in both the matrix and fiber phases [22-26].

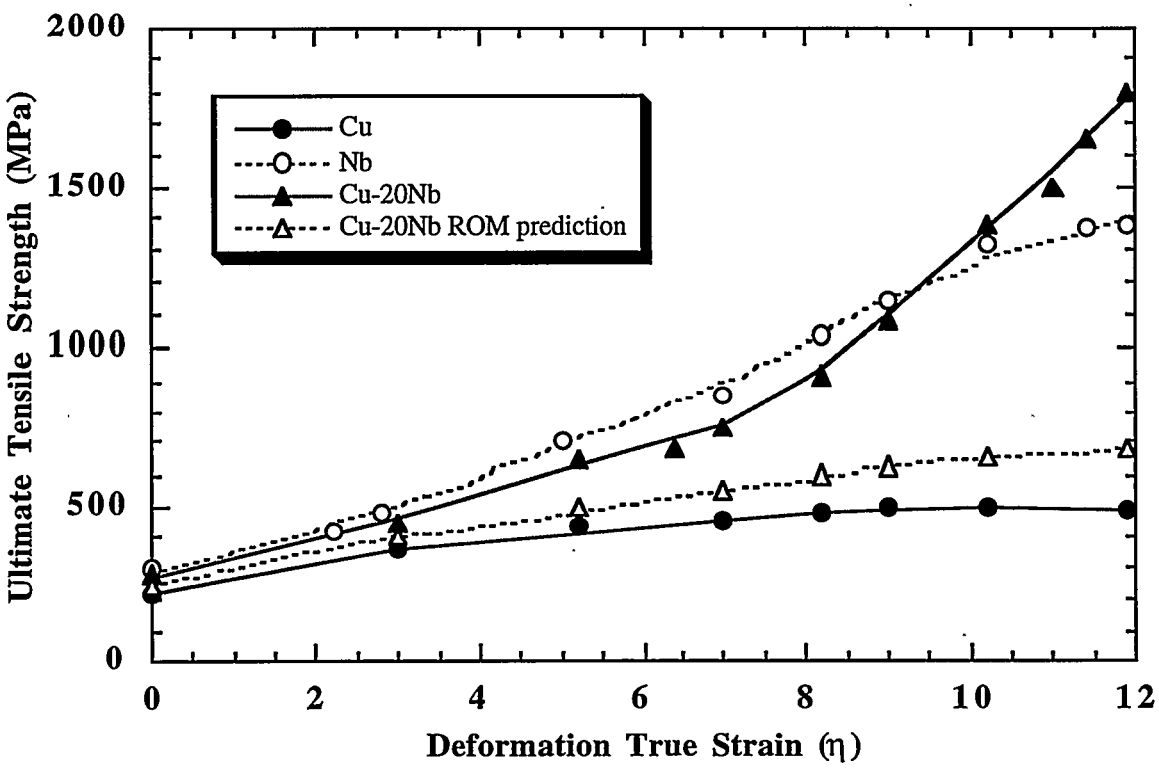

Figure 1 - Effect of draw ratio or rolling reduction on the ultimate tensile stress of Cu, Nb, and Cu-20Nb wire compared to the ROM predictions [24].

Figure 2 shows a representation of the filament morphology typically seen in transverse sections of heavily deformed DMMC rod and sheet materials. Deformation often produces ribbon-shaped filaments that remain parallel to the rolling plane in sheet materials or that become convoluted about the deformation axis in rod materials. These filaments have very high aspect ratios and the microstructure can be classified as being a continuously reinforced composite material. Figure 3 shows a TEM micrograph of heavily deformed Cu-20Nb wire with the folded-ribbon morphology. The ribbon-shaped filaments result from the development of specific textures in the matrix and/or fiber phases during deformation which limit the deformation of the phase to plane strain and will be discussed later.

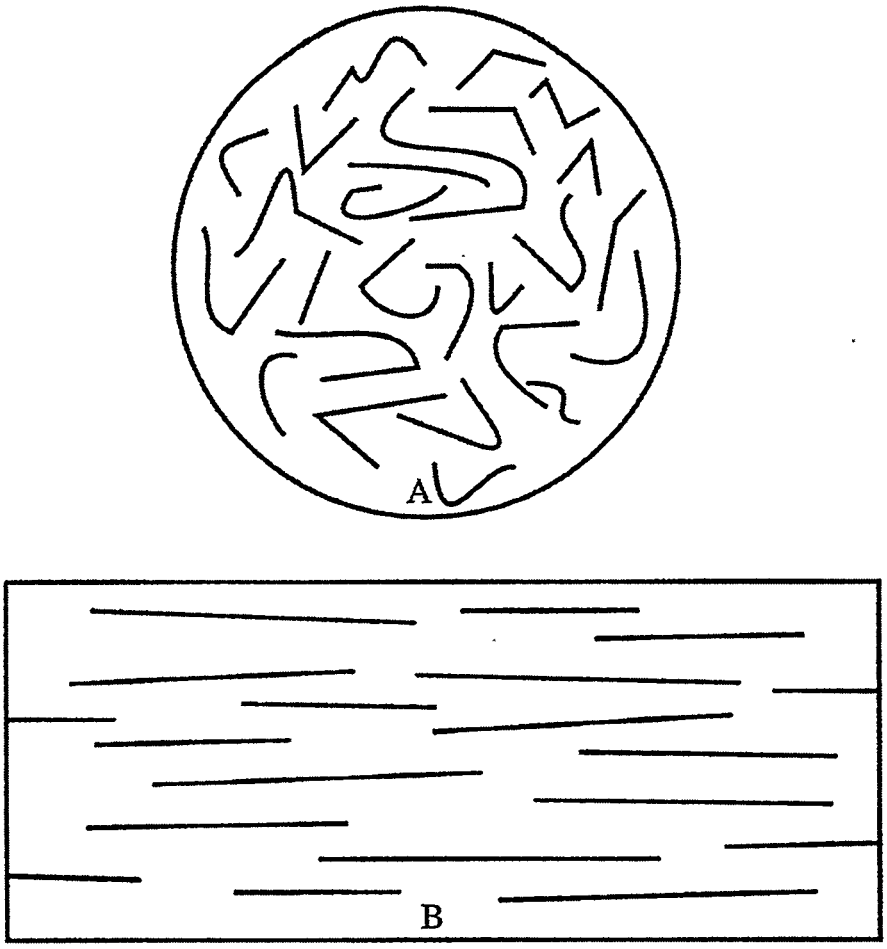

Figure 2 - Filament morphology typically seen in transverse sections of DMMC's. The ribbon-shaped filaments (A) are most common in heavily deformed rod materials and the longitudinal filaments (B) in sheet materials. [19]

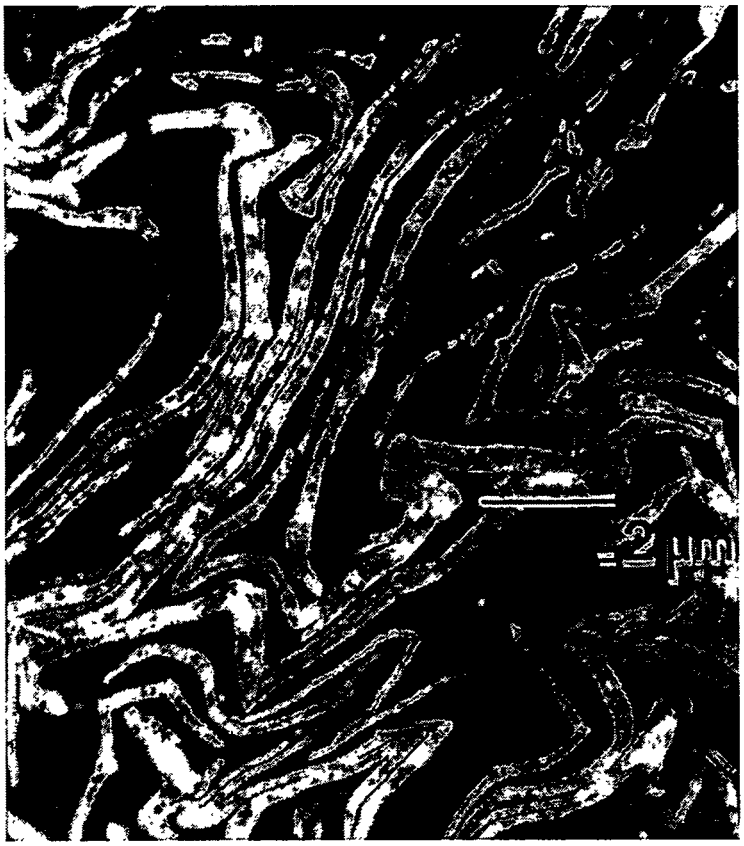

Figure 3 - TEM conical scanning dark-field image of transverse section of wire made from Cu-20 vol.%Nb alloy drawn to $\eta = 9.8$. The bright filaments are Nb and the dark matrix is Cu. [33]

1.3 Ti-Y composites

In an effort to extend the use of deformation processing to non-cubic systems, researchers have studied HCP/HCP Ti-Y composite materials [13-16]. A Ti-20Y composite was deformation processed to a strain of $\eta = 12.8$ by extrusion and drawing with 700°C stress relief anneals performed after each 60% reduction in area. The composite displayed a progressively finer microstructure with increasing amounts of deformation. The as-cast microstructure was characteristic of two immiscible metals (Figure 4). Initial hot work changed the original dendritic structure to a filamentary structure similar to that observed in Cu-X in-situ composites. The size and spacing of the kinked, ribbon-shaped filaments decreased with continuing deformation up through $\eta = 7.27$, resulting in a nanofilamentary microstructure (Figure 5) with an average Y phase thickness of 41 nm at $\eta = 7.27$.

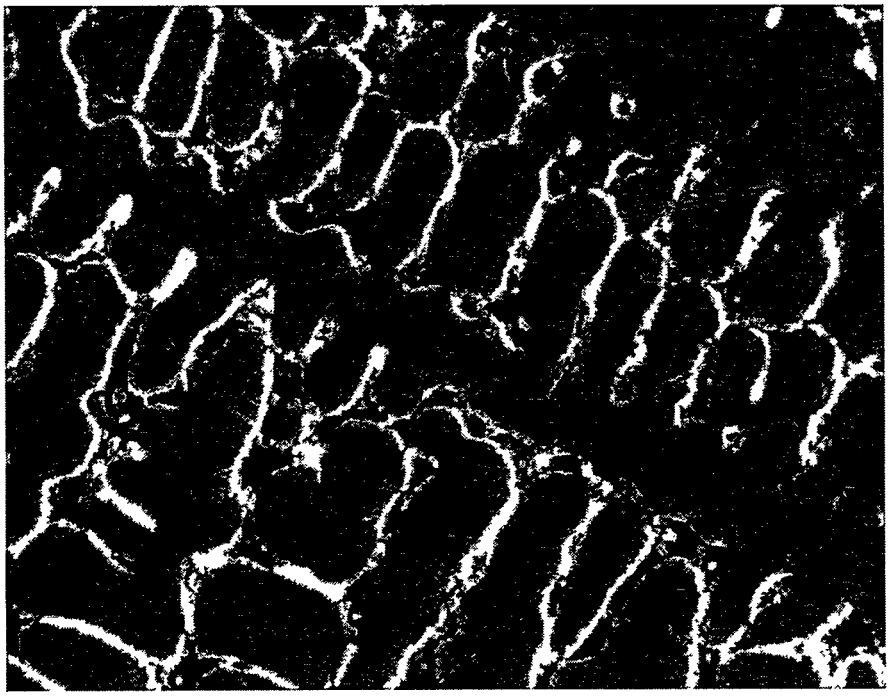

Figure 4 - Scanning electron microscope (SEM) back-scattered electron micrograph of as-cast Ti-20Y. The dark phase is Ti; the light phase is Y (pitted in places by the polishing agents).

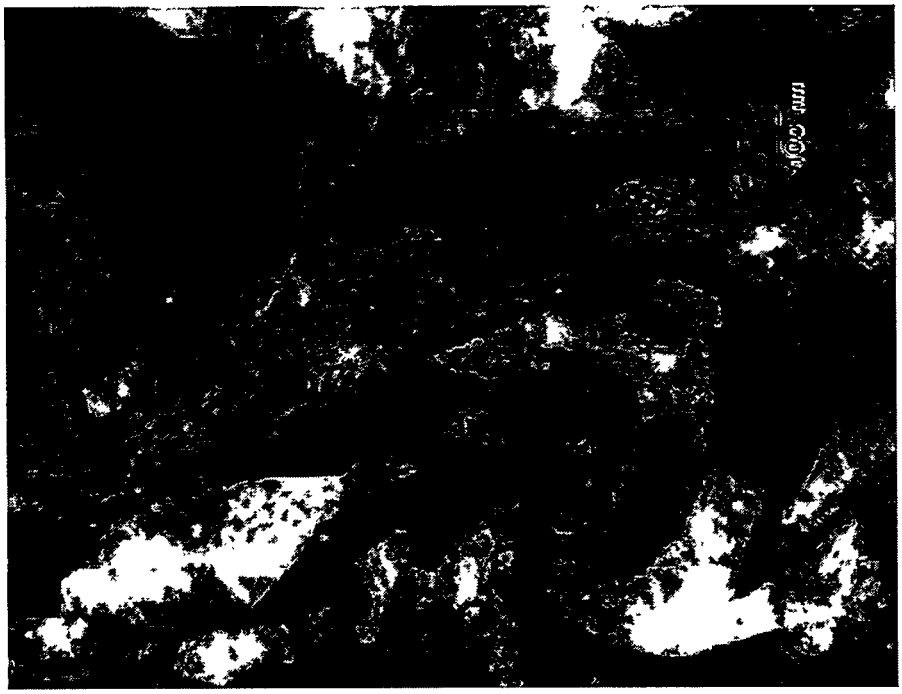

Figure 5 - Conical scan dynamic dark field TEM micrograph of Ti-20Y deformation processed by extrusion, swaging, and drawing to $\eta = 7.27$ and sectioned transversely.

Table 1. Average phase sizes measured by optical microscopy (OM), scanning electron microscopy (SEM), and transmission electron microscopy (TEM) for Ti-20Y.

True Strain (η)	Ti-20Y Average Ti Phase Thickness (μm)	Ti-20Y Average Y Phase Thickness (μm)
0	9.60 (SEM)	2.40 (SEM)
2.25	3.80 (SEM)	0.96 (SEM)
5.03	0.69 (TEM)	0.17 (TEM)
7.27	0.16 (TEM)	0.041 (TEM)

At the highest levels of deformation ($\eta > 9$), the Ti and Y phases developed an equiaxed grain structure that resulted from recrystallization during the many stress relief anneals. Annealing was required to prevent the wire from breaking during further cold working. However, the large surface area of the matrix and fiber phases provided a large driving force for recrystallization during annealing. Further deformation produced the filamentary structure previously observed, but the strength of the material did not increase significantly.

For the Ti-20Y material in the range $2.25 \leq \eta \leq 7.27$, a distinctive folded ribbon microstructure forms with progressively smaller phase thicknesses as the deformation increases, as shown in Table 1. This microstructure is very similar to that seen in the Cu-X deformation processed composites.

Deformation processing more than tripled the UTS of the Ti-20Y composite wire drawn to $\eta = 7.27$ (Figure 6), where the folded-ribbon microstructure was observed. At higher values of η, the phases recrystallized into approximately equiaxed grains, and the strength decreased. Ductilities were relatively high for all the Ti-20Y specimens, ranging from 36% to 63% reduction in area at the fracture surface. The Y second phase also improved the machinability of the Ti-20Y composite as compared to pure Ti. The Ti-20Y machining characteristics were qualitatively similar to those of mild steel.

1.4 Crystallographic texture in Ti-Y and Cu-X composites

X-ray texture pole figures taken on the as-cast Ti-20Y showed no significant texture. But a $<10\bar{1}0>$fiber texture was observed in transverse sections of the deformed rod materials for both the Ti and Y phases throughout the deformation range $2.25 \leq \eta \leq 7.27$. The $<10\bar{1}0>$ fiber texture is normally observed in drawn Ti [28]; its occurrence in drawn Y has

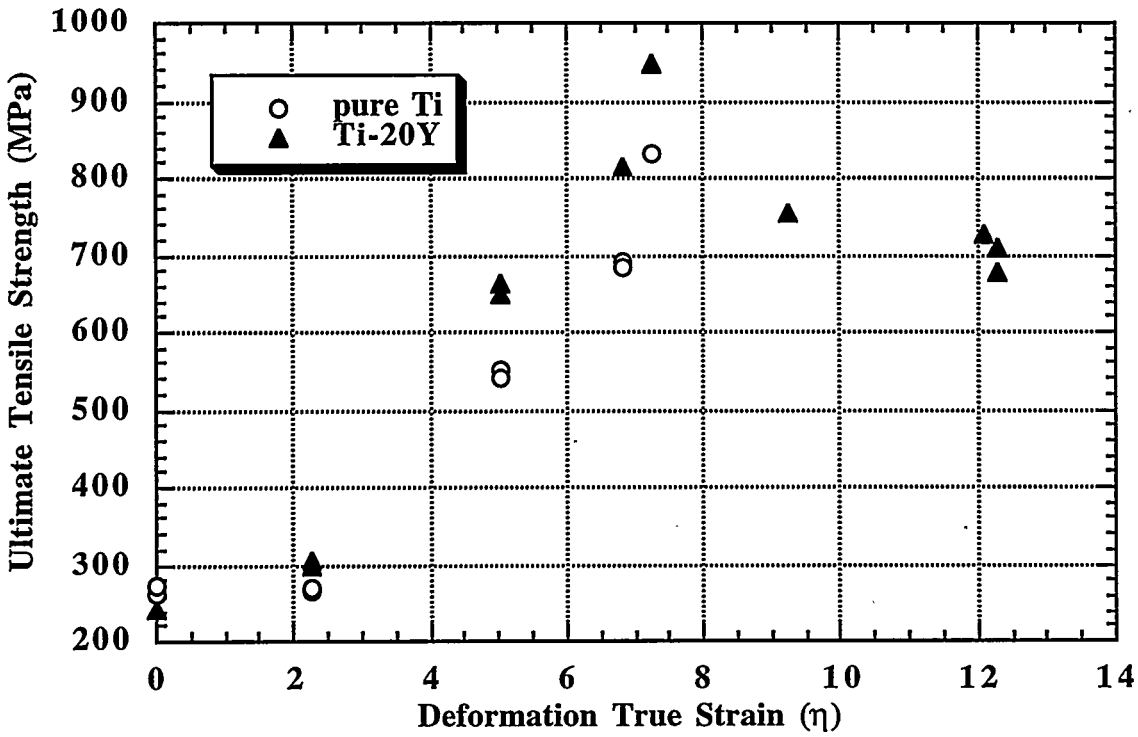

Figure 6. Ultimate tensile strength versus deformation processing of Ti-20Y wire deformed at room temperature with periodic 700°C anneals. The second generation material was hot worked at 700°C to from $\eta = 5$ to $\eta = 5.7$ and then cold worked with 600°C stress recovery anneals.

been less thoroughly studied but seems a likely texture for Y since it has a c/a ratio identical to that of Ti [29].

In Cu-Nb rod materials, the BCC Nb phase typically develops a <110> fiber texture while the Cu matrix develops a <111> and/or <001> fiber texture [30-33]. In a BCC crystal with a <110> fiber texture, two of the four <111> directions ($[1\bar{1}1]$ and $[\bar{1}11]$) are positioned perpendicular to the fiber axis and thus cannot slip. All slip is limited to the remaining two <111> directions ([111] and $[11\bar{1}]$) which lie opposite one another across the specimen center line, thus limiting deformation in the BCC phase to plane strain [1, 34]. (See Figure 7). The FCC Cu matrix, however, can readily deform axisymmetrically with either the <111> or <001> fiber texture, since these orientations possess three and four active slip directions, respectively. The Cu-X DMMC materials are therefore characterized by plane-straining BCC

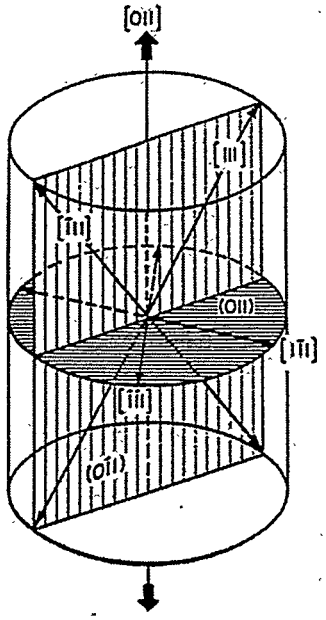

Figure 7 - Schematic diagram of the four slip directions in a BCC material with a <110> preferred orientation. Only two of the four <111> directions can accommodate extension parallel to the wire axis, resulting in plane-strain deformation. [2, 31]

filaments embedded in a Cu matrix with multiple slip systems that can accommodate the limited deformation mode of the fibers.

The axisymmetrically-deforming FCC Cu which surrounds the plane-straining BCC phase constrains the filaments and results in the curling effect seen in Figure 3. That is to say, the overall specimen geometry remains cylindrical during deformation to comply with the deformation of the bulk material. Thus, for an equivalent amount of deformation, FCC/BCC Cu-X DMMC materials have a much thinner effective filament thickness and a much larger matrix/fiber interfacial area than do FCC/FCC deformation processed composites such as Ag-Cu or Ag-Ni. The deformation processed Ag-Cu wire of Frommeyer and Wassermann was comprised of 100% FCC phases which both deform axisymmetrically, and these specimens achieved much lower maximum UTS values (1250 to 1400 MPa) even at filament thicknesses as small as 12 to 25 nm [35]. It has been suggested that the presence of a plane straining phase resulting in the convoluted microstructure seen in Cu-Nb is one of the reasons for the superior strength of the FCC/BCC DMMC materials [1].

There is a striking similarity between the arrangement of available slip systems in an HCP crystal with a $< 10\bar{1}0 >$ fiber texture and in a BCC crystal with a <110> fiber texture. Both situations limit slip to two directions which are bisected by the center line of the rod (as compared to the three or four slip directions possible in a textured FCC lattice), so both

crystals are limited to a plane strain deformation mode. This analysis would predict that a DMMC material comprised of HCP metals would undergo the same filament shaping processes that have been observed in the BCC filaments of Cu-X composites. Since both the Ti and Y phases are limited to plane strain in a $< 10\bar{1}0 >$ fiber texture orientation, the folded-ribbon shape seen in the BCC filaments of Cu-X composites would be expected for both phases in the Ti-Y composite. This, in fact, has been observed in Ti-20Y composite wires [13-16]

The exceptionally large interfacial boundary area present in such plane-straining microstructures (as seen in Cu-X and Ti-Y) might also explain the anomalous strengthening observed in FCC/BCC Cu-X composites but absent in FCC/FCC composites such as Ag-Cu [32]. The increase in strength observed for the Ti-20Y composite in Figure 6 is quite similar to that observed in the Cu-20Nb composites over the range $0 \leq \eta \leq 7.27$ [1, 4].

As previously mentioned, the Ti-20Y composites did not maintain the desired folded-ribbon microstructure at strains greater than $\eta = 7.27$. The greatest improvement in the mechanical properties of Cu-X composites occurred at the highest true strains where filament thicknesses were reduced to less than 10 nm. The Ti-20Y specimens either recrystallized when high annealing temperatures were used or broke apart during deformation when lower annealing temperatures were used [13-16]. One possible explanation for the observed inability of the Ti-20Y composite to tolerate very large strains is the geometric challenge of fitting two plane straining phases into a cylinder whose radius diminishes as deformation progresses. It may simply be impossible to fit two plane-straining, ribbon-shaped phases into a contiguous, void-free cylindrical arrangement at high true strains [11, 18].

1.5 Conductivity and strength of deformation processed composites

Research on deformation processed Cu-X alloys, where X is a BCC element, has shown [1, 2] that wires of this material can be produced that have better combinations of strength and electrical conductivity than are available in the best commercial copper alloys. When X elements that have significant solubility in copper are used, a severe reduction in conductivity occurs. In a study of Cu-15 vol% Cr alloys [37], the conductivity of the alloys dropped monotonically with temperature upon heating, except over a range from around 400-500°C where it rose significantly (Figure 8). The rise results from the precipitation of Cr, which had been quenched into metastable solid solution in the copper matrix in the chill casting. (When one heated the as-cast sample back up to 810°C after the first heat cycle, it followed the upper curve on both heat-up and cool-down.)

In this same study, conductivity was measured as a function of temperature for a deformation processed alloy. The curve followed the same path as the cast material. But it was found that for higher deformation, the chromide precipitation occurred at a lower temperature (Figure 8). Also, the room temperature conductivity decreased with increasing UTS and η. (Figure 9).

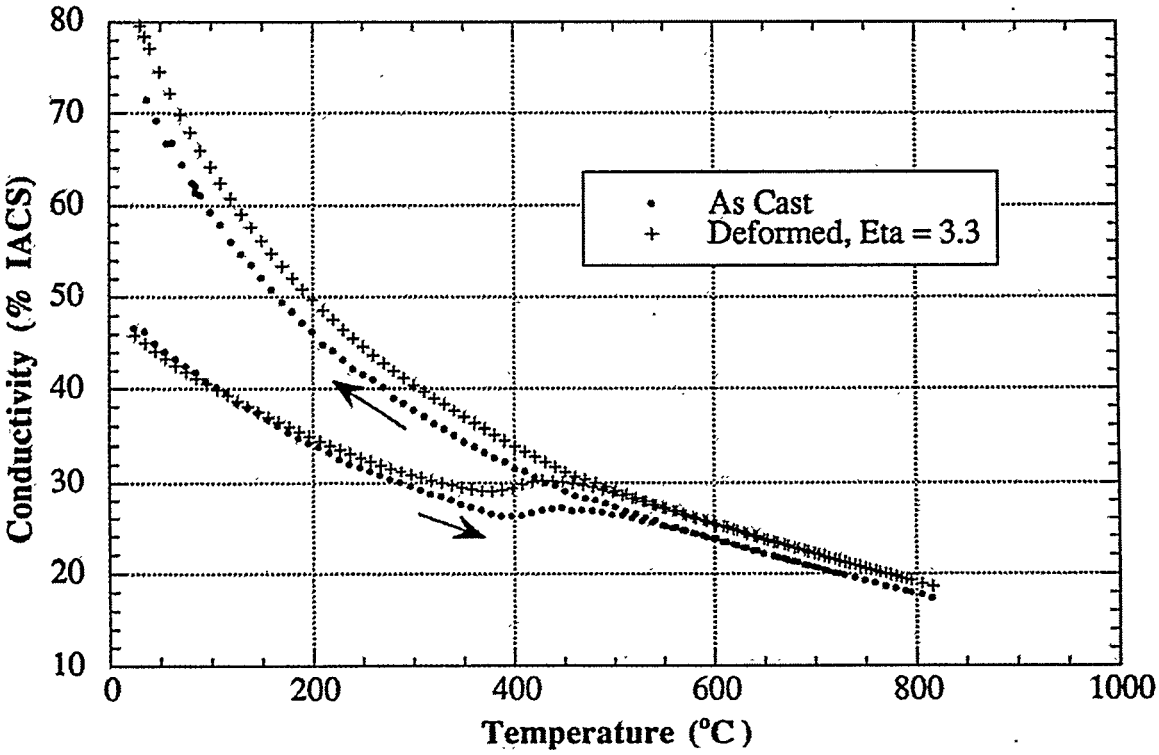

Figure 8 - Electrical conductivity versus temperature plot for two Cu-15 vol% Cr alloys heated to and cooled from 810°C. [37]

1.6 Statement of work

The objective of this study is to find a light weight, high strength, high conductivity, low corrosion alloy that can be drawn to a long wire, and also used at high temperatures. A potential use is for power generation in space shuttles where a long wire is flown through the magnetic field of the earth to generate power. Another potential use is high voltage power lines, although the cost would be a limiting factor.

Based on the given criteria, a DMMC Al-20Ti alloy was chosen. Aluminum was chosen because of its high conductivity, good ductility, light weight and low corrosion, and titanium because of its high strength-to-weight ratio and good corrosion resistance. Another

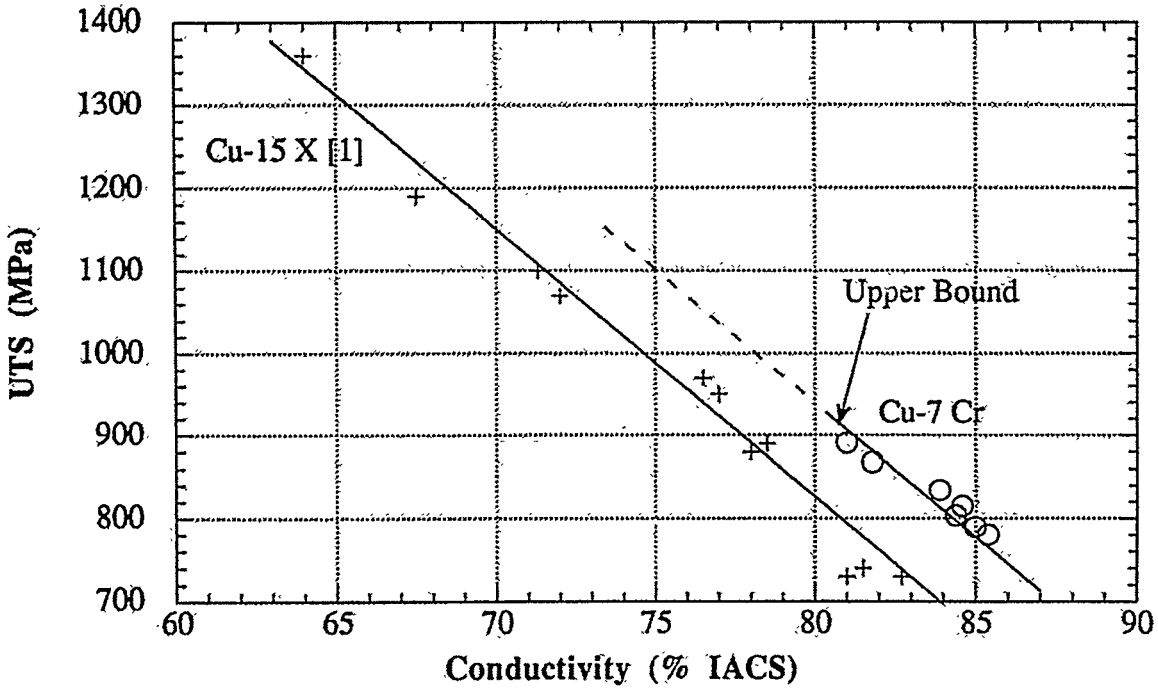

Figure 9 - Strength versus conductivity of Cu-7 vol.% Cr data compared to literature data on Cu-15 vol.% X (where X = niobium, tantalum, and chromium). [37]

favorable feature with this alloy is that the electrode potentials of the pure Al (E°= -1.662V) and Ti (E°= -1.630) are so close that the chance to get an internal galvanic cell is negligible.

An exposure of the Al-20Ti DMMC to high temperature would be expected to react the two pure metals to form Al_3Ti intermetallic compound in an Al matrix. Since Al_3Ti is a refractory equilibrium phase in the Al-Ti system with a melting temperature of 1623 K and a much higher elastic modulus (166 GPa) than Al, deformation processing Al-Ti powder mixtures may offer a moderate-cost method of forming bulk quantities of nano-scale Al + Al_3Ti composites with superior strength and high temperature resistance. Formation of Al_3Ti is an exothermic reaction, so DTA will be used to determine the temperature where this equilibrium phase forms at various amounts of deformation. XRD is used to confirm the DTA results.

The electrical resistivity of pure Ti is rather high for a metal (ρ=420 nΩ·m), but 80% of the cross sectional area of the DMMC is expected to be long strands of high-purity Al (ρ=26.5 nΩ·m at 300 K) which form a parallel conduction path with the Ti filaments. The contribution of the preferred orientations of the Al and Ti filaments to the electrical resistivity was assumed to be nil at 300 K, based on the findings of Hashimoto [43]. Both room temperature and high temperature electrical resistivity measurements will be done on

the alloy to determine whether the Ti-filaments will have a significant effect on the conductivity.

The microstructure of the Al-20Ti DMMC is expected to be similar to the Al-20Nb DMMC of Thieme. The Al-20Nb has a plane straining second phase in a very ductile Al FCC matrix, and displays a large increase in strength as the second phase spacing and thickness decrease. Since the high strength of a DMMC is due to the texture and microstructure, both tensile testing, microscopy and texture analysis will be done on the alloy.

2 EXPERIMENTAL PROCEDURE

Al powder (99.99% purity, 780 wt. ppm O) of particle size 45-75μm produced by the Ames Laboratory gas atomized rapid solidification (GARS) process (Figure 10) was blended with Ti powder (99.4% metal basis purity, 150μm maximum particle size, containing 675 wt. ppm O and 50 wt. ppm N). (Figure 11) These metal powders were blended and CIP'ed at 14 MPa pressure to form a green compact of 80 vol.% Al and 20 vol.% Ti (71 wt.% Al - 29 wt.% Ti). The 37mm diameter CIP'ed (Cold Isostatic Pressing) compact was loaded into a Ta-foil-lined, OFHC Cu can which was electron beam welded shut *in vacuo* to protect the specimen from atmospheric contamination during subsequent hot extrusion and room temperature swaging operations. The specimen in its Cu can was heated for 1 hour in a furnace at 535 K then extruded through a heated 13 mm diameter die followed by water quenching (Figure 12). The temperature for extrusion was selected to be high enough to enhance ductility for the extrusion yet low enough to avoid the reaction of the Al and Ti to form the equilibrium Al_3Ti phase (Figure 13).

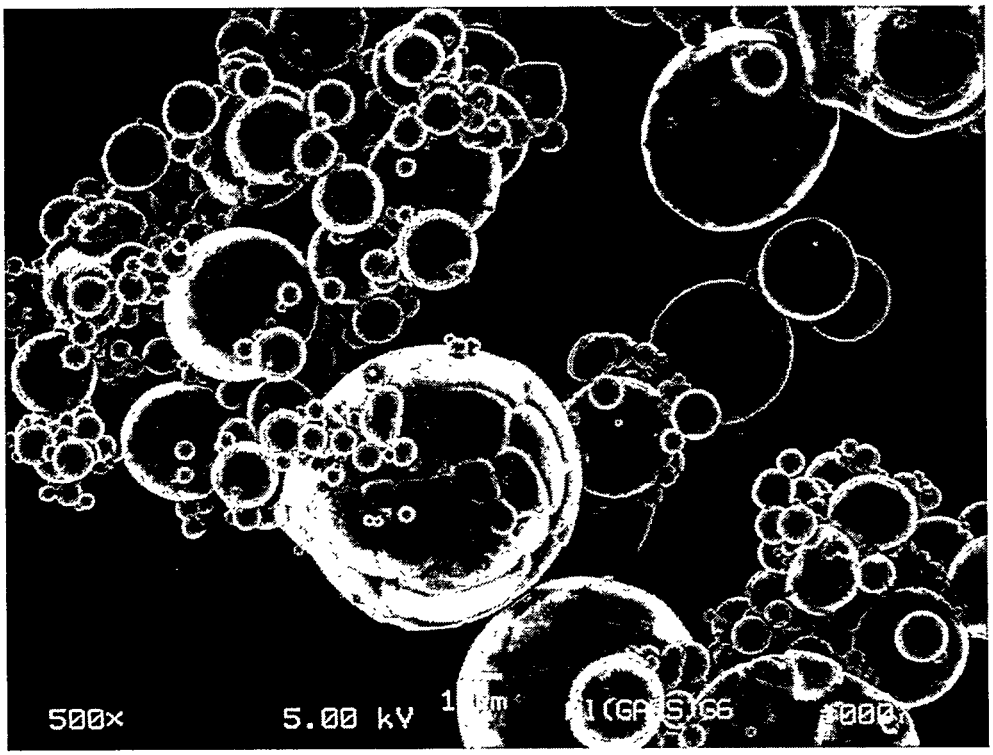

Figure 10 - Aluminum powder produced by the Ames Laboratory gas atomized rapid solidification (GARS) process.

Figure 11 - Titanium powder used to make the CIP'ed compact of Al-20Ti.

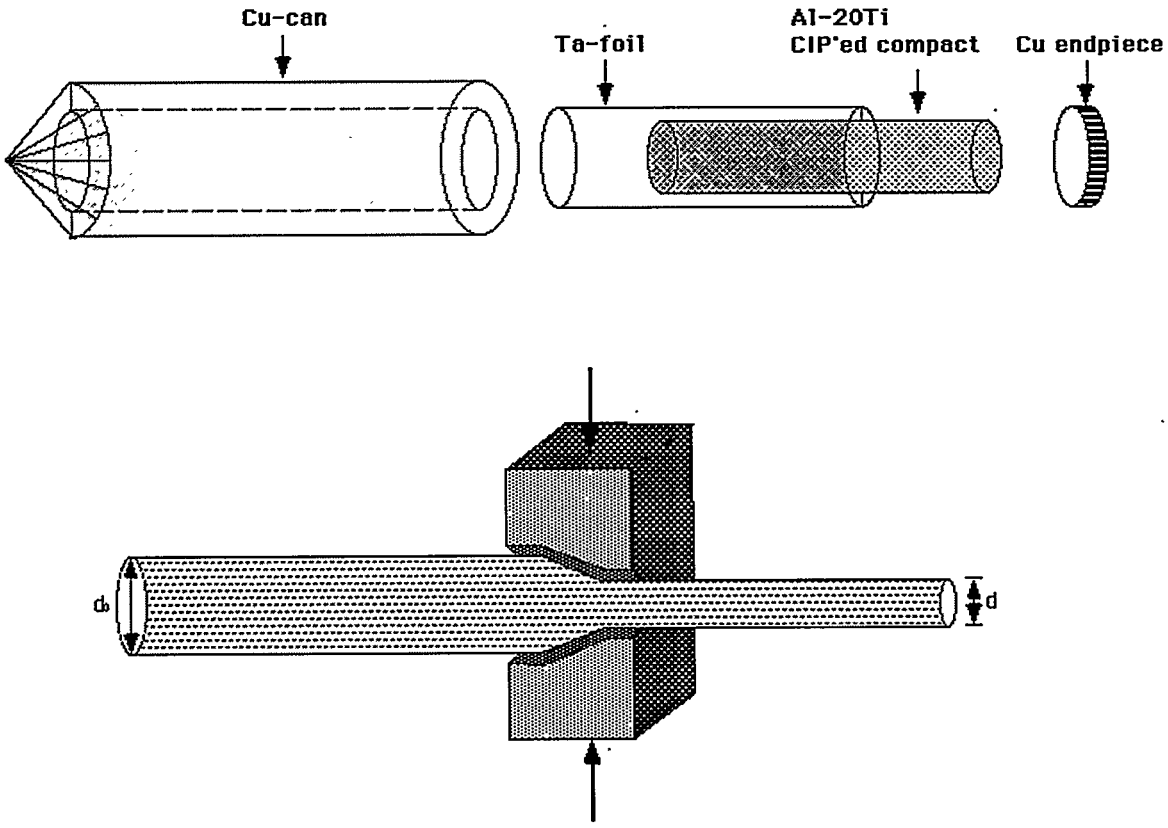

Figure 12 - Schematic of the preparation, and extrusion of the Al-20Ti alloy.

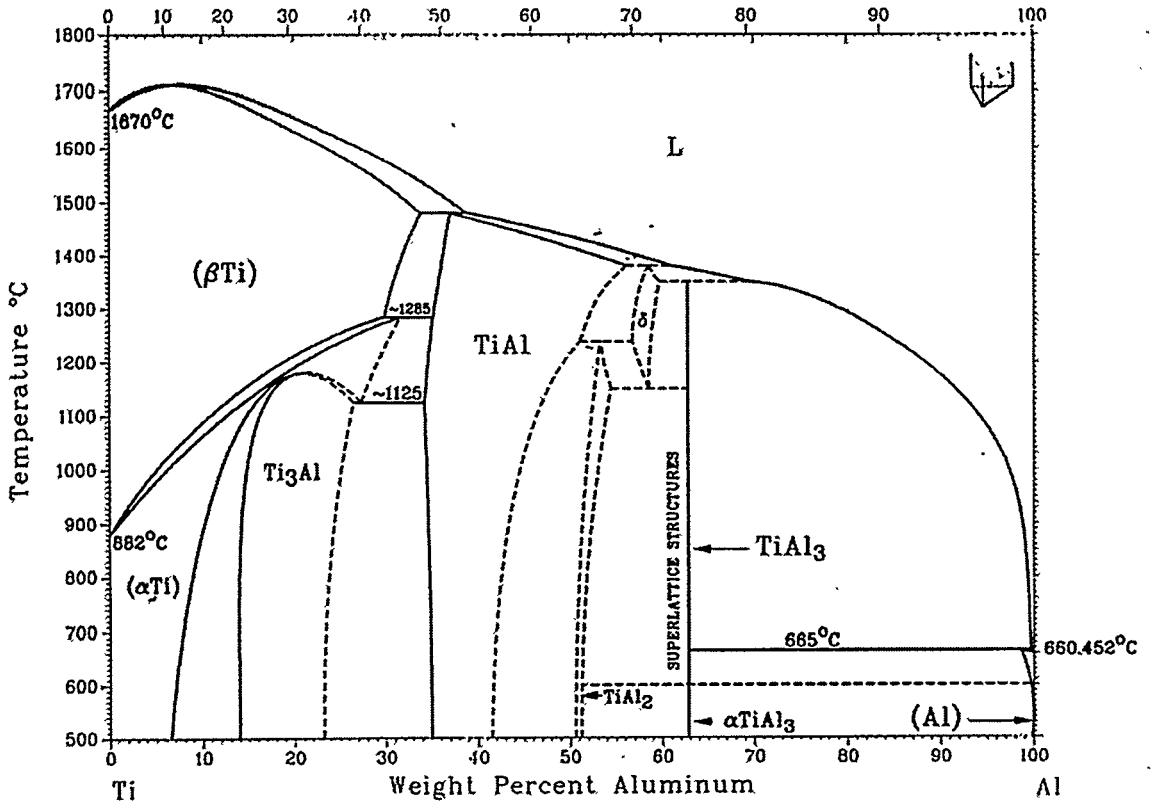

Figure 13 - Equilibrium binary phase diagram for Ti and Al [38]. The equilibrium phases of the Al_{GARS}-20Ti is Al_3Ti and Al.

The true strain of the specimen was calculated using:

$$\eta = 2\ln\frac{d_o}{d_f} \quad \text{where, } \eta = \text{true strain, } d_o = \text{original diameter, and } d_f = \text{final diameter}$$

The extruded rod with Cu sleeve ($\eta = 2.5$) was swaged at 300 K to a diameter of 8 mm. At this point the Cu and Ta were removed by machining. The bare Al-20Ti specimen was then swaged to a final diameter of 2.5 mm ($\eta = 5.1$). A small metallography coupon and two tensile specimens with the tensile axis parallel to the rod axis were cut from the specimen at $\eta = 2.5$ and at $\eta = 5.1$.

The 2.5 mm diameter rods were cleaned, cut into 90 mm lengths, and bundled inside another Ta-foil-lined, OFHC Cu can. This Cu can was electron beam welded *in vacuo* to seal the specimens inside, and this 51 mm outside diameter, 140 mm long Cu can was heated for 1 hour in a furnace at 535 K then extruded through a heated 13 mm diameter die followed by water quenching. This second extrusion bonded the many separate specimen rods into a

single piece with an effective deformation true strain of 7.7. The extruded rod was then swaged to a diameter of 8 mm, at which point the Cu and Ta were removed by machining. The bare Al-20Ti specimen was then swaged at 300 K to a diameter of 2.5 mm (η=10.3). A small metallography coupon and two tensile specimens with the tensile axis parallel to the rod axis were cut from the specimen at η=7.7 and at η=10.3. A small portion of the 2.5 mm diameter η=10.3 material was wire drawn at 300 K to a final diameter of 1.0 mm (η=12.1). Several tensile specimens, electrical resistivity specimens, and a metallography specimen were prepared from the η=12.1 material.

An attempt was made to re-bundle the η=10.3 material and extrude it a third time. This procedure failed, and it was found by XRD that the extruded rod had reacted to form a two-phase material of Al and Al_3Ti microstructure. This material was too brittle to tolerate further deformation processing.

3 TESTING PROCEDURES USED ON THE AL-20TI COMPOSITE

3.1 Introduction to testing procedures

Six tests were performed on the Al-20Ti specimens at several points in the deformation processing sequence:

1. Tensile testing to measure mechanical properties (ultimate tensile strength and ductility as per cent reduction in area).
2. X-ray diffraction texture analysis and orientation imaging microscopy (OIM) to measure preferred crystallographic orientation.
3. X-ray diffraction analysis to find the phases present.
4. Scanning electron microscopy (SEM) and transmission electron microscopy (TEM) to measure phase size and shape
5. Resistivity measurement to measure electrical properties as a function of temperature and deformation.
6. Differential thermal analysis (DTA) to measure phase changes as a function of temperature

3.2 Tensile testing procedures

Tensile testing procedures for specimens in the range $\eta = 2.5$ to 10.3 followed ASTM Standard E8 [37], which requires a 4:1 ratio between the length and the diameter of the specimen gauge length. The highest deformed sample (η=12.1) had a too small diameter to allow the 4:1 ratio. All tensile test specimens were simply machined in a lathe around the cylindrical specimen axis until ASTM E8 geometry was attained. Specimen gauge lengths were polished with 500-mesh abrasive paper to eliminate lathe tool marks around the gauge length circumference. All specimens were tensile tested at room temperature on Instron 1125 and Instron 4505 tensile testing machines at a strain rate of 0.0085mm/s except for the smallest diameter samples (η=12.1) which were pulled at a strain rate of 0.0042mm/s. A minimum of two tensile specimens were made for each η value.

For all tensile tests, a value of engineering ultimate tensile strength (UTS) was calculated from the quotient of the applied maximum load and the initial cross sectional area of the specimen (UTS = load / area). Ductility was calculated for each specimen by measuring the area of the fracture surface in a traveling microscope and comparing that area to the original cross sectional area of the specimen to calculate the per cent reduction in area.

3.3 Texture analysis procedures

3.3.1 X-ray diffraction texture analysis

Transverse cross section specimens were cut from the Al-20Ti composite at deformation levels of $\eta = 2.5$, 7.7, and 10.3. X-ray texture specimens were not prepared for specimens with $\eta > 10.3$ due to the difficulty in preparing a transverse section of fine wires with a large enough area to produce a strong diffraction signal. Each specimen was metallographically polished through a 1/4-μm abrasive.

The polished specimens were mounted on a Philips PW1078/50 texture goniometer, and an initial 2 theta scan from 30° to 90° was made with unfiltered Cu x-rays to locate diffraction peaks. Each diffraction peak corresponds to a particular plane of diffraction in the Al or in the Ti. Several of these diffraction peak angles were then selected for pole figure measurements of x-ray texture of that particular plane's orientation with respect to the specimen's rod axis. Data acquisition and analysis were performed by a Philips APD1700 Automated Powder Diffraction System. Each pole figure was acquired using a 5mm sample lateral oscillation and a 5° per spiral psi pitch, where psi is the radial angle of the pole figure. Measurements were begun at psi = 0° and halted at psi = 80°.

3.3.2 Orientation Imaging Microscopy procedures

Transverse cross section specimens were cut from the Al-20Ti composite at deformation levels of $\eta = 2.5$, 7.7, and 10.3. Each specimen was metallographically polished through a 1/4-μm abrasive. An attempt was made to achieve a deformation free sample preparation procedure. Initially a light perchloric etch was used in order to remove the amorphous surface layer to produce a better signal for the OIM. However, the samples had a thick amorphous layer, so this attempt was unsuccessful. After several trials, a method was found that gave a higher confidence level: The sample was polished through a 1/4-μm abrasive followed by ion milling for about 3 hours at 3.5 kV and with 0.5 mA ion current. A careful polishing through a 1/4-μm abrasive followed by mechanically polishing a long time with a very light hand on the last two polishing wheels also gave a positive result. Preparation procedures that were tried but did not produce the desired result included mechanical polishing followed by electropolishing, and various acid etches (Kroll's reagent, hydrofluoric acid, and perchloric acid).

OIM pole figures were generated from electron back-scatter diffraction patterns (EBSP's) obtained with an Amray 1845 field-emission gun SEM and equipment developed

by TexSEM Laboratories (TSL). The EBSP's were analyzed using TSL's software running on a Silicon Graphics Inc. (SGI) Indy workstation. The pole figures were obtained using the Auto Hough algorithm option.

3.4 X-ray diffraction analysis procedures

X-ray diffraction analysis was done on the initial powders (Al and Ti) and on the as-extruded sample (η=2.5) both before and after heat treatment for 24 hours at 600°C (Above the reaction temperature for Al + Ti $\rightarrow$ Al_3Ti). An XRD pattern was also obtained from the failed 3rd extrusion to determine if any reaction had occurred and to find what phases were present. All XRD patterns were obtained using a Phillips 1700 series diffractometer, and 2 theta scans from 20° to 120° were made with filtered Cu x-rays (Ni filter) to locate diffraction peaks.

3.5 Microscopy procedures

Microscopy samples were made for both scanning electron microscopy (SEM) and transmission electron microscopy (TEM) to measure phase spacings and to allow visual inspection of the phase morphology. SEM specimens were prepared at deformation levels of η = 2.5, 5.1, 7.7, 8.5, 10.3 and 12.1. Both transverse and longitudinal cross section samples were made for most of these samples. The samples were mounted in metallographic mounts and polished through a 1/4-μm diamond abrasive wheel with the final three polishing steps performed on oil-based abrasive suspensions (rather than water-based) to avoid any possible reactions between the aluminum and water. The large difference in atomic numbers of Ti (22) and Al (13) provided excellent contrast between the two phases in the back-scattered electron (BSE) imaging mode, and consequently no chemical etch was needed to show the phase boundaries in the SEM. A Cambridge S-200 unit operated at accelerating voltages of 15kV to 20kV was used for imaging these samples.

TEM samples were prepared for the highest deformation levels (η = 10.3 and 12.1). Sample discs of the η = 10.3 were cut transversely with a diamond cut-off wheel, mechanically thinned on a VCR Groop Dimpler and further thinned to perforation on a Gatan 600 ion mill using argon ions. The η = 12.1 specimen diameter was too small to permit direct sectioning, so four lengths of the wire were bundled together inside a 3 mm diameter stainless steel tube. The tube with the wires was then filled with epoxy glue and held under vacuum for a few seconds to permit air to flow out of the tube so it would fill completely with epoxy (Figure 14). When the epoxy was set, the sample was cut into 3mm size discs

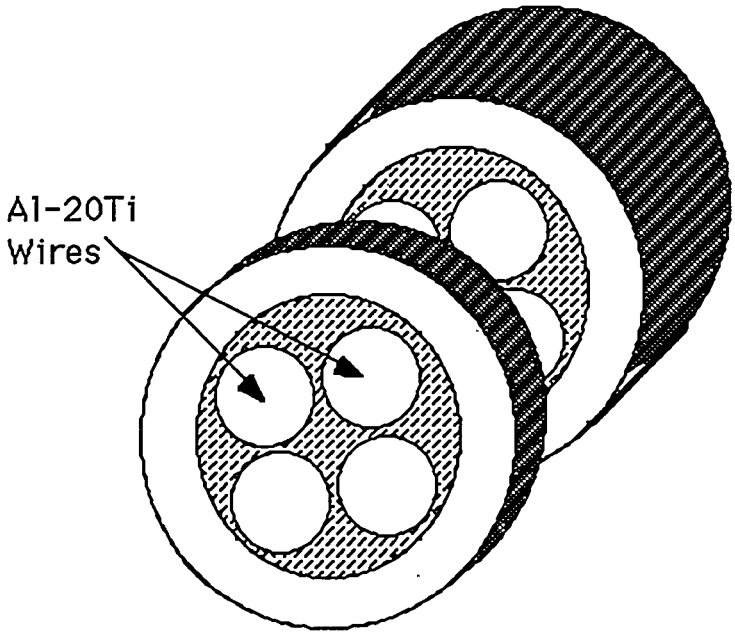

Figure 14 - Preparation of Al-20Ti TEM sample from η = 12.1 wires.

and prepared as the η = 10.3 sample. Both samples were studied in the TEM, a Philips CM30 S/TEM unit operated at 300kV accelerating voltage.

3.6 Resistivity measurement procedures

The electrical resistivity, ρ, of the specimens at η=12.1 was measured at 300 K both before and after an 86,000 s (24 hours) recovery anneal at 473 K *in vacuo*, and the ultimate tensile strength of specimens at η=12.1 was also measured both before and after an 86,000 s (24 hours) anneal at 473 K *in vacuo*.

Four point resistance of the samples was measured using a Keithley 580 micro-ohmmeter operating in the pulse mode to eliminate thermal EMF's. The samples were in the form of drawn wires of uniform cross sectional area. Small grooves were machined into each sample for the application of voltage sense probes. Source current probes were clipped to the ends of the samples. Three different methods of applying sense probes were used. Two related methods relied on clips or point contacts inserted into the machined grooves. The third method involved wrapping 0.004 inch diameter Ta wire into the grooves and spot welding the wire in place. Voltage probe leads were then clipped onto the Ta wires. Four resistance measurements were obtained and averaged for each sample. The measured resistance, R, was converted to resistivity by

$$\rho = \frac{RA}{d}$$

where ρ is the resistivity, A is the cross sectional area of the wire computed from the measured diameter (D), and d is the distance between voltage probes. For sample 1, D=0.096 cm and d= 0.81313 cm. For sample 2, D=0.100 cm and d=0.80787 cm. Four resistance measurements at elevated temperatures were performed in vacuum with a procedure described by Cook et al. [45]

3.7 Differential thermal analysis procedures

Differential thermal analysis (DTA) was done on samples of η = 2.5, 7.7, 8.5, 10.3 and 12.1 in a Perkin Elmer DTA 7 apparatus with an alumina crucible. For all samples, the heating rate was 10°C/min, and the heating was done in argon atmosphere to avoid oxidation of the samples. Approximately 50 mg of sample was heated to 655°C. The difference in temperature between the sample and a reference (alumina powder) was measured as a function of increasing temperature in the furnace. This method can show features like glass transitions, crystallization, melting, and oxidation, and gives a good sense of the thermal reactions that may occur in the sample at various temperatures.

4 RESULTS AND DISCUSSION

4.1 Tensile test results

Tensile testing was done at all the stages of deformation to measure how the strength depended on deformation. Previous study on Cu-X [1-10] and other DMMCs [11-16] show anomalous strengthening as deformation is increased. Tensile testing was done to see if the Al-20Ti alloy also would show this same increase in strength.

The tensile strength of the Al_{GARS}-20Ti specimens increased several-fold as the deformation processing proceeded. The relation between true strain and ultimate tensile strength is plotted in Figure 15, and the data for the figure are tabulated in Table 2. The strength increases and the ductility decreases with increasing deformation. Although the material still showed considerable ductility at the highest η's, stress relief anneals at 400°C for 2 hours on two tensile samples of true strain 5.1 showed a decrease in ultimate tensile strength (UTS = 128MPa and 122Mpa, respectively). A similar heat treatment, at 200°C for 24 hours, on two tensile samples of η=12.1 showed no significant change in tensile properties (UTS = 577MPa and 611MPa).

Table 2 - Ultimate tensile strength and ductility values measured at 300 K for various levels of deformation true strain in Al-20Ti DMMC.

True Strain (η)	Ultimate Tensile Strength (MPa)	Ductility as Percent Reduction in Area
2.5	131	36%
2.5	144	20%
5.1	184	28%
5.1	186	23%
7.7	235	29%
7.7	242	32%
10.3	345	27%
10.3	366	28%
12.1	586	20%
12.1	606	13%

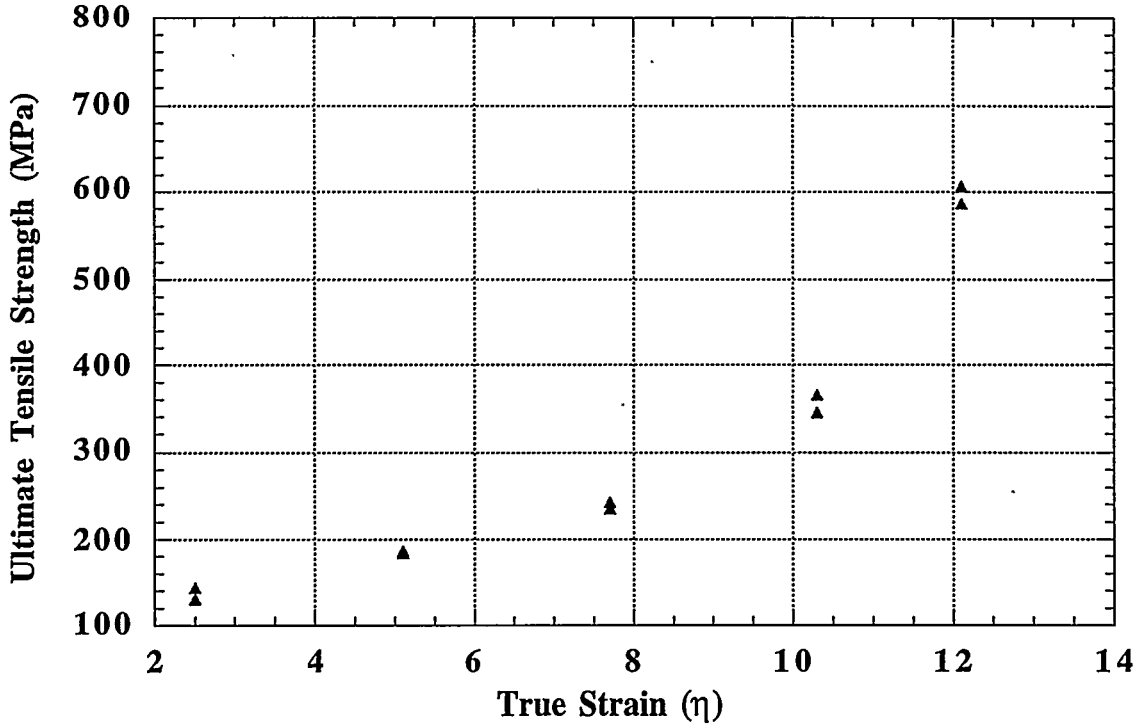

Figure 15 - Ultimate tensile strength values measured at 300 K for various levels of deformation true strain in Al-20Ti DMMC.

4.2 X-ray texture measurements and orientation imaging microscopy

The physical properties of many materials are related to the texture. One example is Cu where the elastic modulus is 68GPa along <100>, and 21GPa along <111> [46]. The microstructure of the Al-20Ti alloy can be explained from the texture of the sample; the plane straining of the Ti phase results in the kinked, ribbon-shaped filaments. It is therefore interesting to study the texture of the sample and to see if the texture varies with deformation.

Texture analysis of XRD and OIM pole figures for the Al_{GARS}-20Ti rod confirms the $< 10\bar{1}0 >$ fiber axis orientation typically seen in axisymmetrically deformed Ti [41]. The XRD texture data (Figures 16-17, 20, 22-23) shows a $< 10\bar{1}0 >$texture, but the OIM pole figure (Figure 29) shows a $< 11\bar{2}0 >$ texture. This is believed to be due to the nature of the two methods used. In OIM, the texture data is taken from a few grains within the sample. The typical area of study is in the range of 0.2-400μm (in this particular case, 100μm of the sample was studied). In XRD texture analysis a larger part of the sample is surveyed (5mm of the sample). So even though areas may have a $< 11\bar{2}0 >$ texture (as in Figure 29), the XRD pole figures showing a $< 10\bar{1}0 >$ fiber axis orientation gives a better average of the texture in the whole sample.

Similarly, OIM pole figures taken from the Al grains (Figures 27-28) deviate some from the XRD texture analysis of the Al (Figures 18-19, 21, and 24-26). The OIM shows areas with a dual <100> and <111> fiber texture (Figure 27) just like the XRD texture data, and other areas with a dual texture of <100> and <110> (Figure 28).

When looking at the wire drawn and extruded samples in the electron microscope (SEM), there is a distinct change between the microstructure of the central area and the edge of the sample (see SEM results, Figure 50). The central part shows the classic convoluted, ribbon-shaped Ti-filaments, while the edges show flat Ti-filaments, a microstructure more commonly seen in sheet material (See Figure 2). This can help explaining the difference between the results from the OIM and the XRD unit. According to Verhoeven [1], the <111> and <100> fiber texture is common in FCC wire drawn and extruded samples, while the <110> fiber texture is common in FCC rolled sheets. For HCP material the $< 10\bar{1}0 >$ fiber texture is common in wire drawn and extruded samples while the $< 11\bar{2}0 >$ fiber texture is common in HCP rolled sheets.

OIM pole figures give more directional information about the sample than XRD texture pole figures. This is due to the size of the area studied. A few grains that are close to each other are more likely to have the same alignment and therefore produce a pole figure that can more easily be compared to a stereographic projection. An average of many grains in an axisymmetrically deformed sample will give a pole figure where the intensity is smeared out in a circle at a given angle from the central spot. An ideally textured sample would show a thin ring of intensity.

In any kind of deformation process there will always be some deviation from an ideal sample. This results not only from the deformation process but also from the cutting and polishing of the sample. If a sample is not cut at perpendicular to the fiber axis, the texture analysis will be in error by the angle at which the cut deviates from the perpendicular. This is taken into consideration when analyzing the pole figure plots, and the texture is given as an average of three different samples (η=2.5, 7.7, and 10.3).

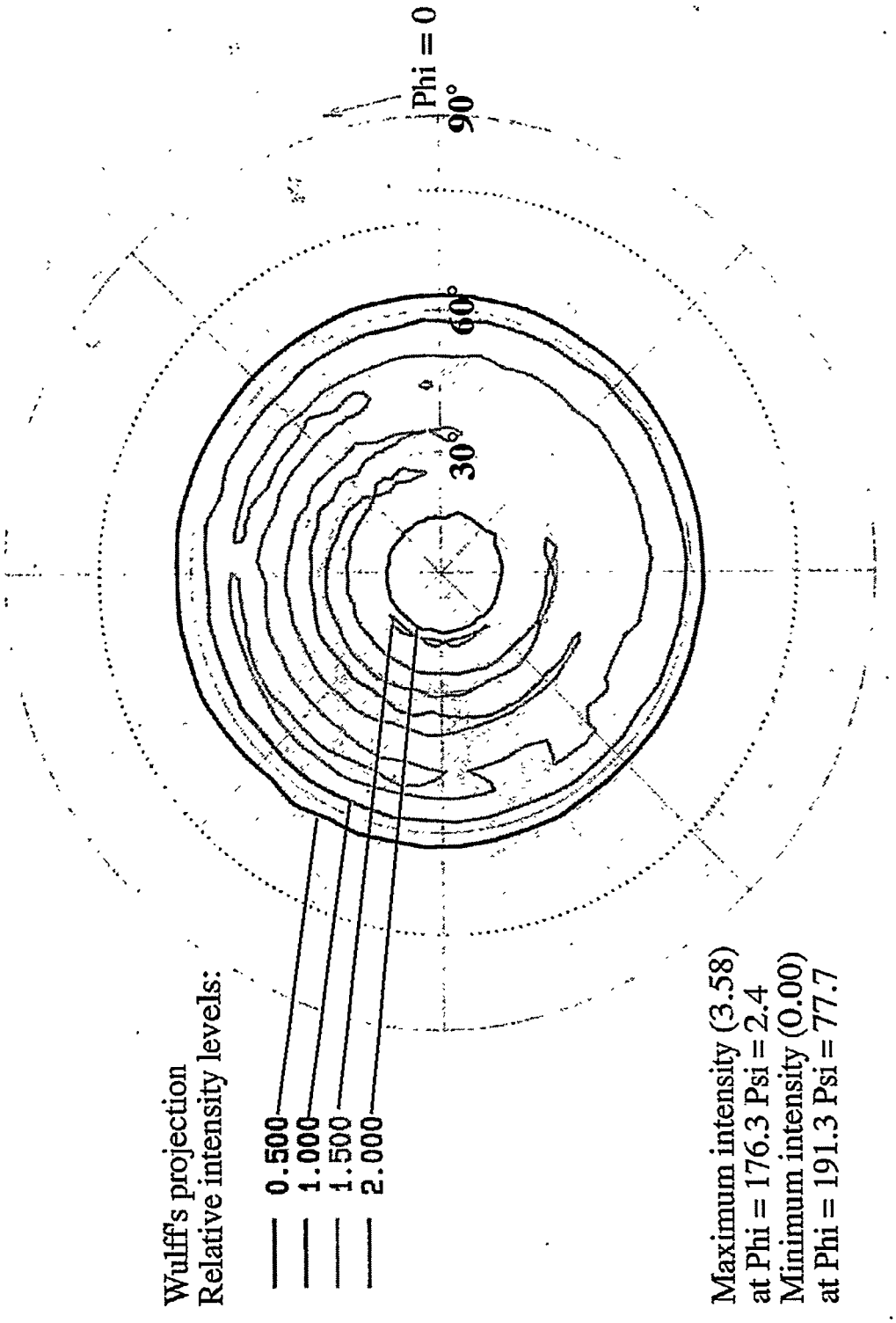
Phi = 0
90°
60°
30°
Wulff's projection
Relative intensity levels:
0.500
1.000
1.500
2.000
Maximum intensity (3.58)
at Phi = 176.3 Psi = 2.4
Minimum intensity (0.00)
at Phi = 191.3 Psi = 77.7

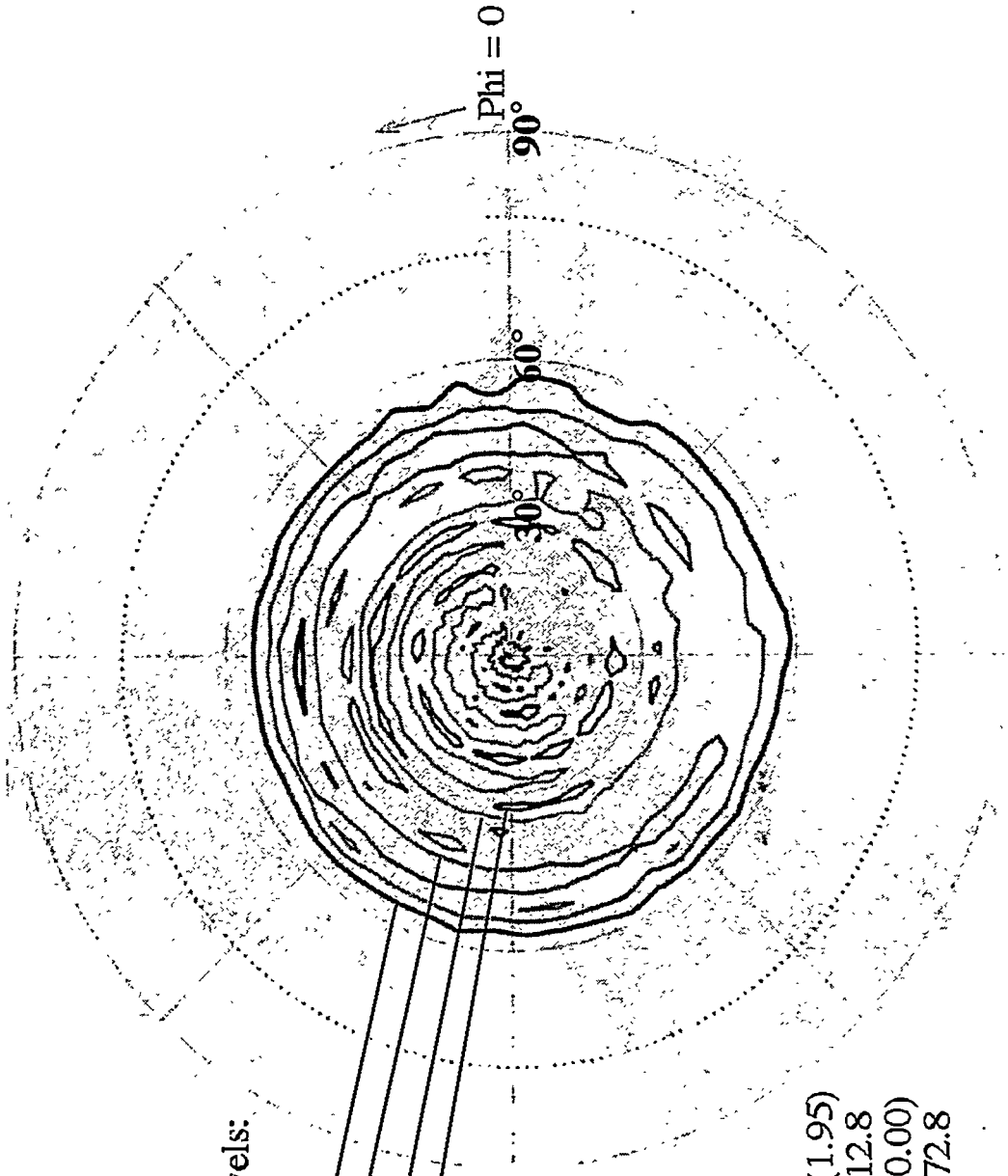
Phi = 0
90°
60°
30°
Wulff's projection
Relative intensity levels:
1.200
1.400
1.600
1.800
Maximum intensity (1.95)
at Phi = 198.8 Psi = 12.8
Minimum intensity (0.00)
at Phi = 198.8 Psi = 72.8

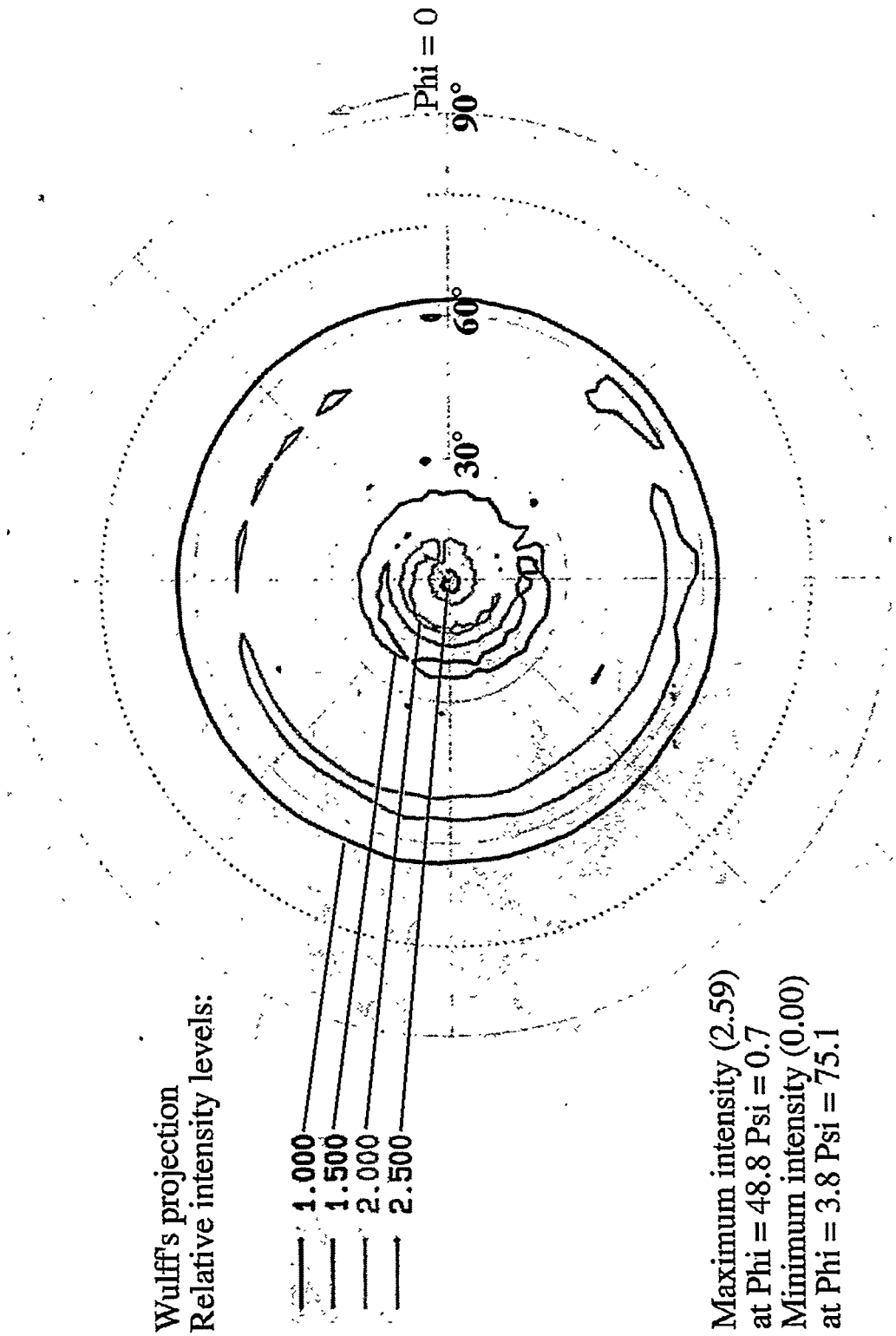
Phi = 0
90°
60°
30°
Wulff's projection
Relative intensity levels:
1.000
1.500
2.000
2.500
Maximum intensity (2.59)
at Phi = 48.8 Psi = 0.7
Minimum intensity (0.00)
at Phi = 3.8 Psi = 75.1

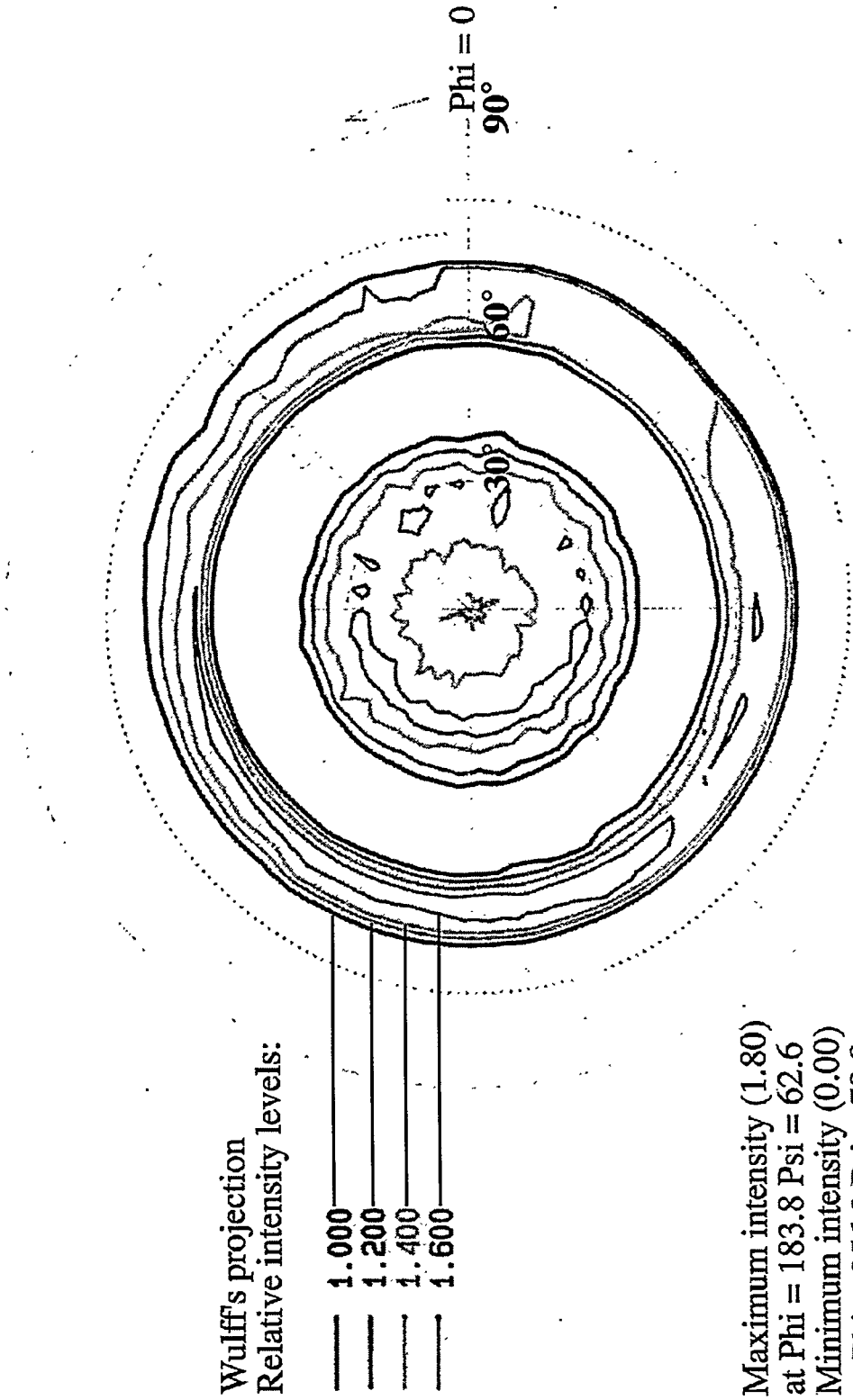
Phi = 0
90°
60°
30°
Wulff's projection
Relative intensity levels:
1.000
1.200
1.400
1.600
Maximum intensity (1.80)
at Phi = 183.8 Psi = 62.6
Minimum intensity (0.00)
at Phi = 356.3 Psi = 79.9

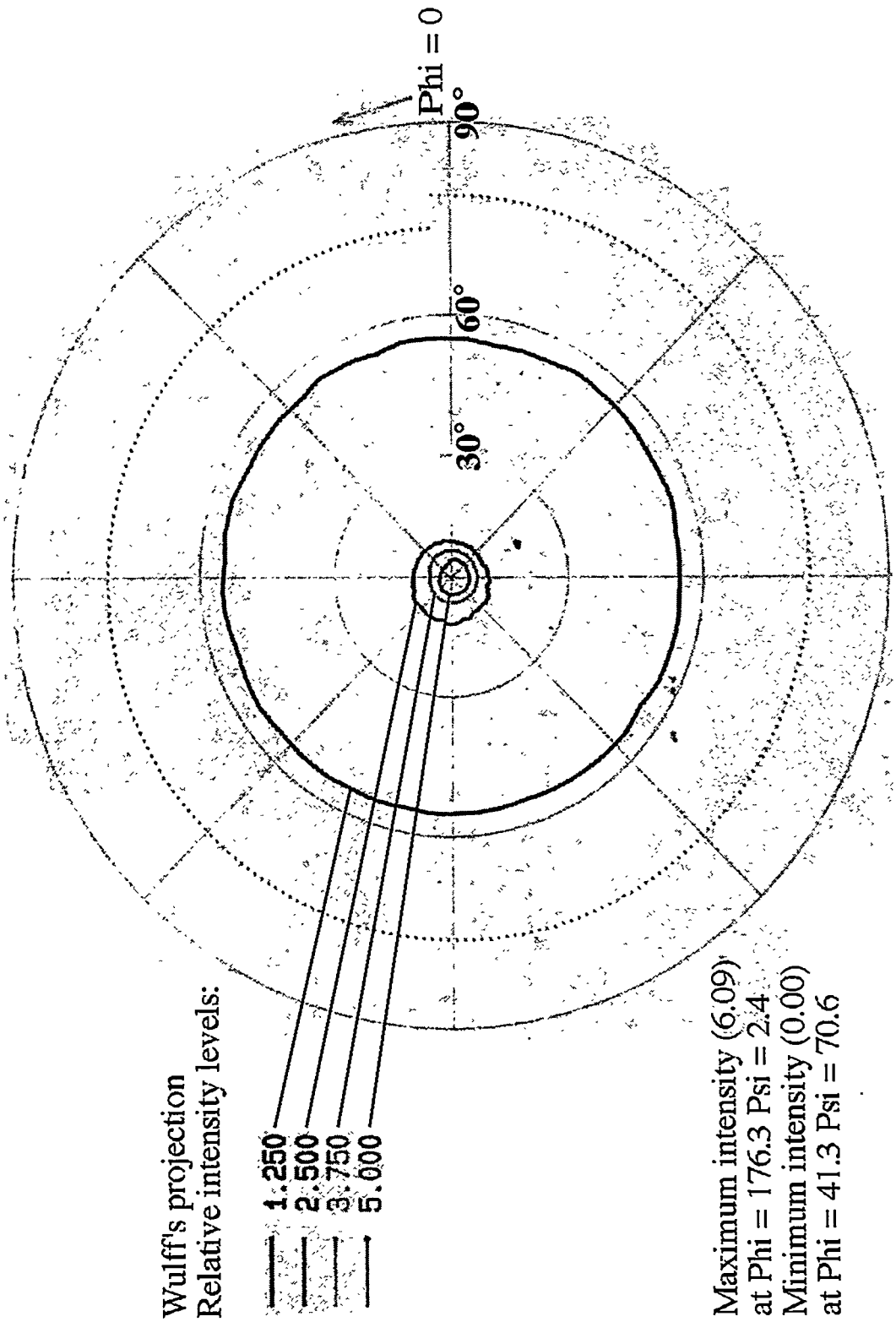
Phi = 0
90°
60°
30°
Wulff's projection
Relative intensity levels:
1.250
2.500
3.750
5.000
Maximum intensity (6.09)
at Phi = 176.3 Psi = 2.4
Minimum intensity (0.00)
at Phi = 41.3 Psi = 70.6

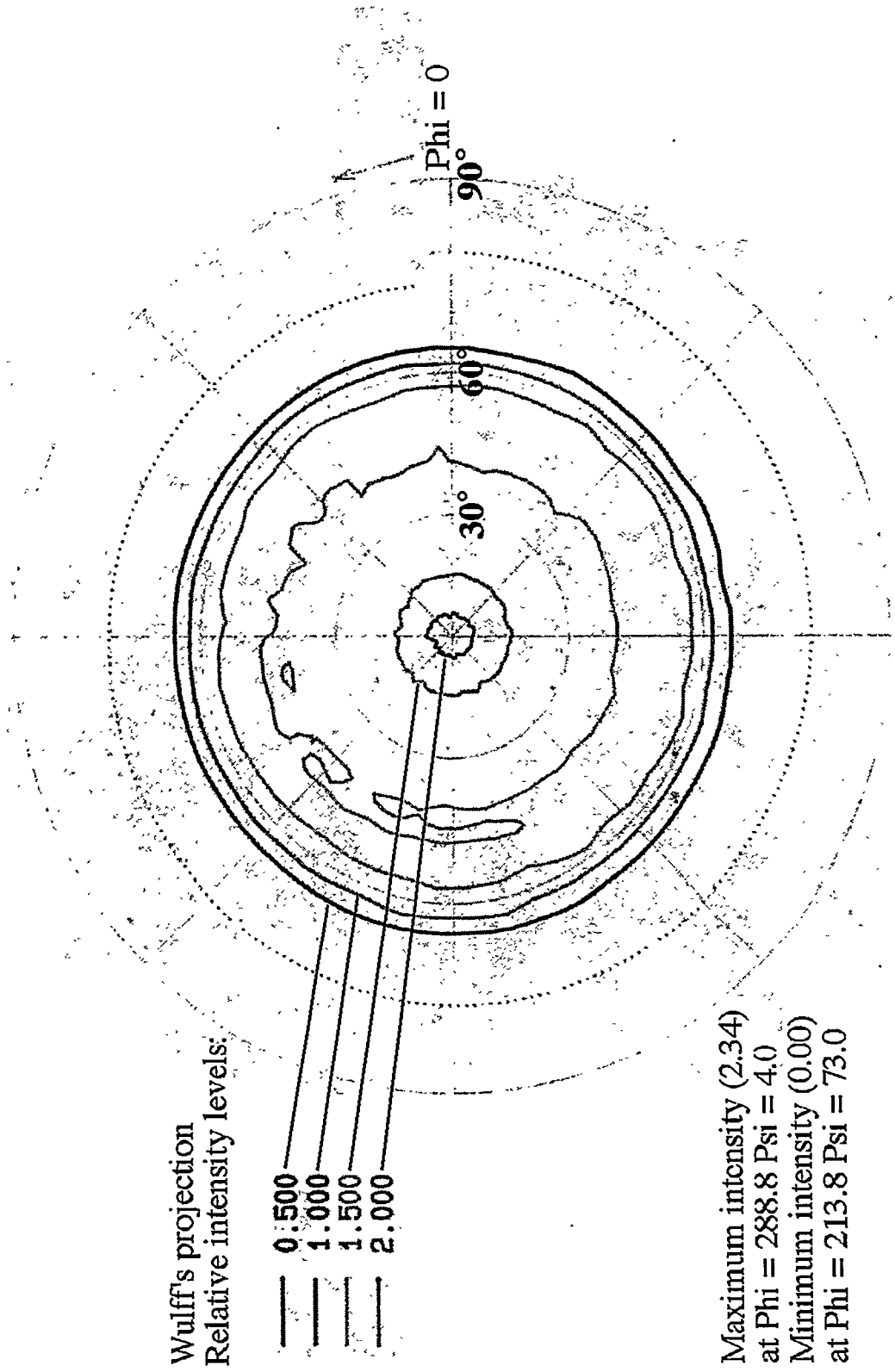
Phi = 0
90°
60°
30°
Wulff's projection
Relative intensity levels:
0.500
1.000
1.500
2.000
Maximum intensity (2.34)
at Phi = 288.8 Psi = 4.0
Minimum intensity (0.00)
at Phi = 213.8 Psi = 73.0

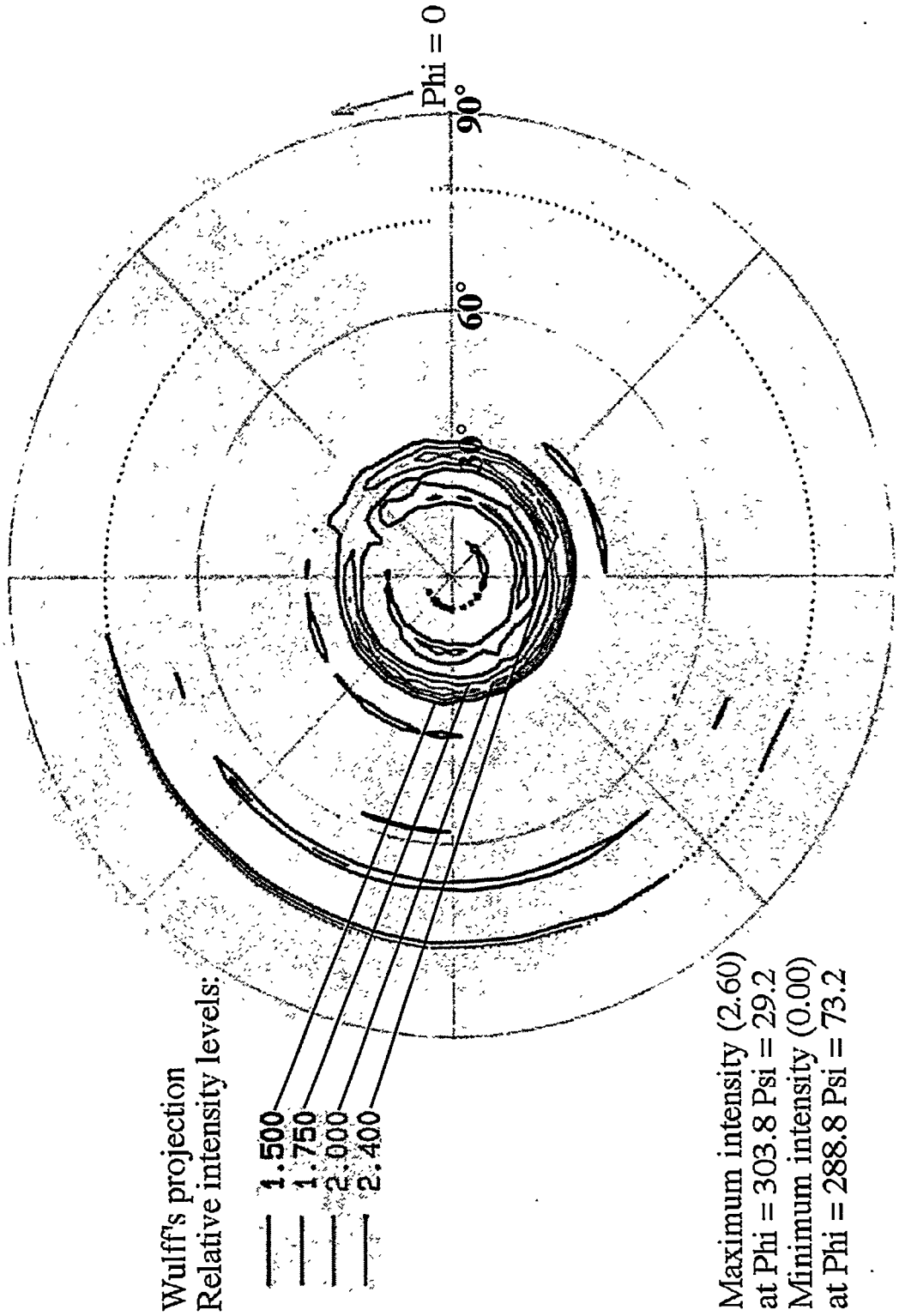
Phi = 0
90°
60°
30°
Wulff's projection
Relative intensity levels:
1.500
1.750
2.000
2.400
Maximum intensity (2.60)
at Phi = 303.8 Psi = 29.2
Minimum intensity (0.00)
at Phi = 288.8 Psi = 73.2

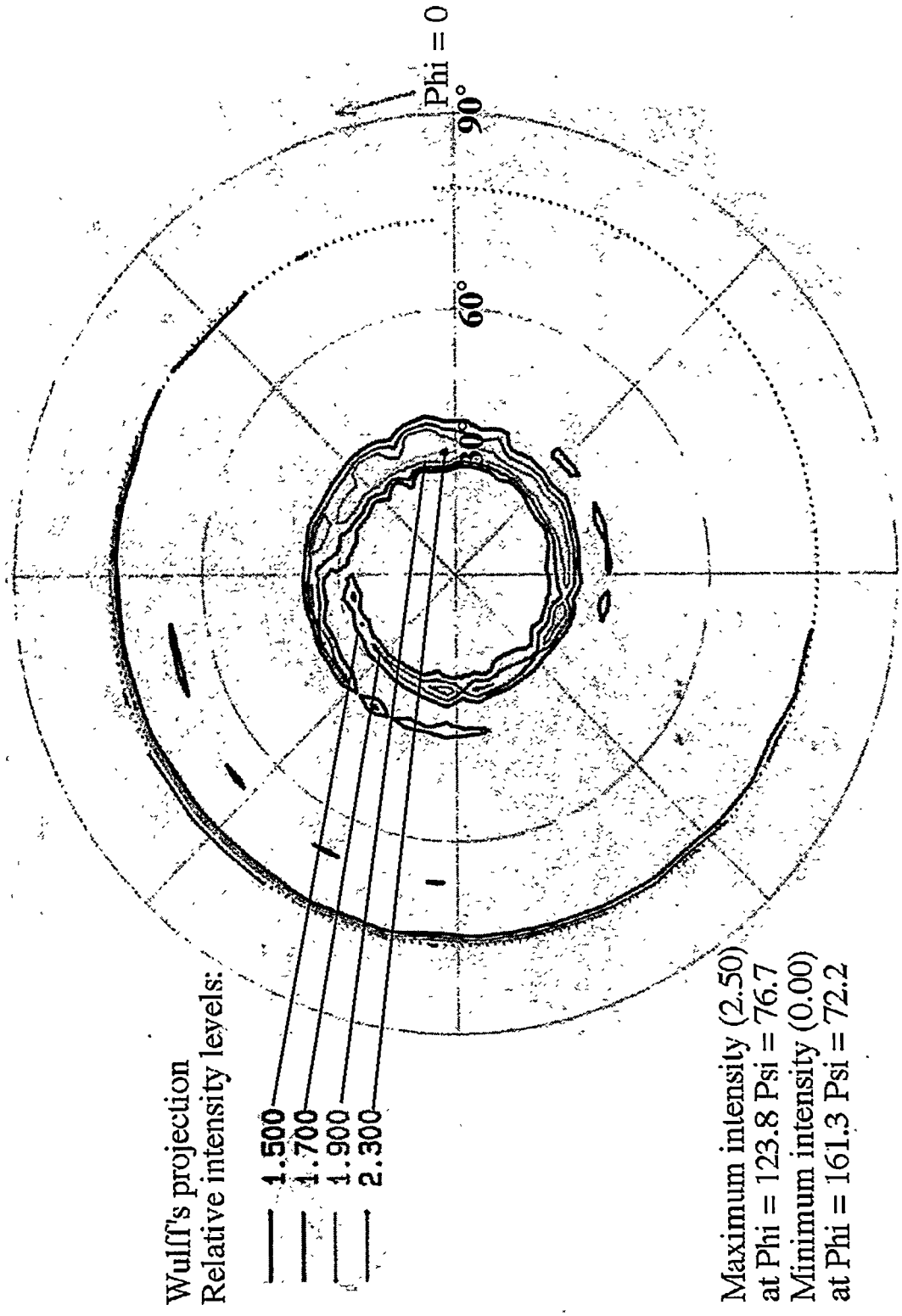
Phi = 0
90°
60°
30°
Wulff's projection
Relative intensity levels:
1.500
1.700
1.900
2.300
Maximum intensity (2.50)
at Phi = 123.8 Psi = 76.7
Minimum intensity (0.00)
at Phi = 161.3 Psi = 72.2

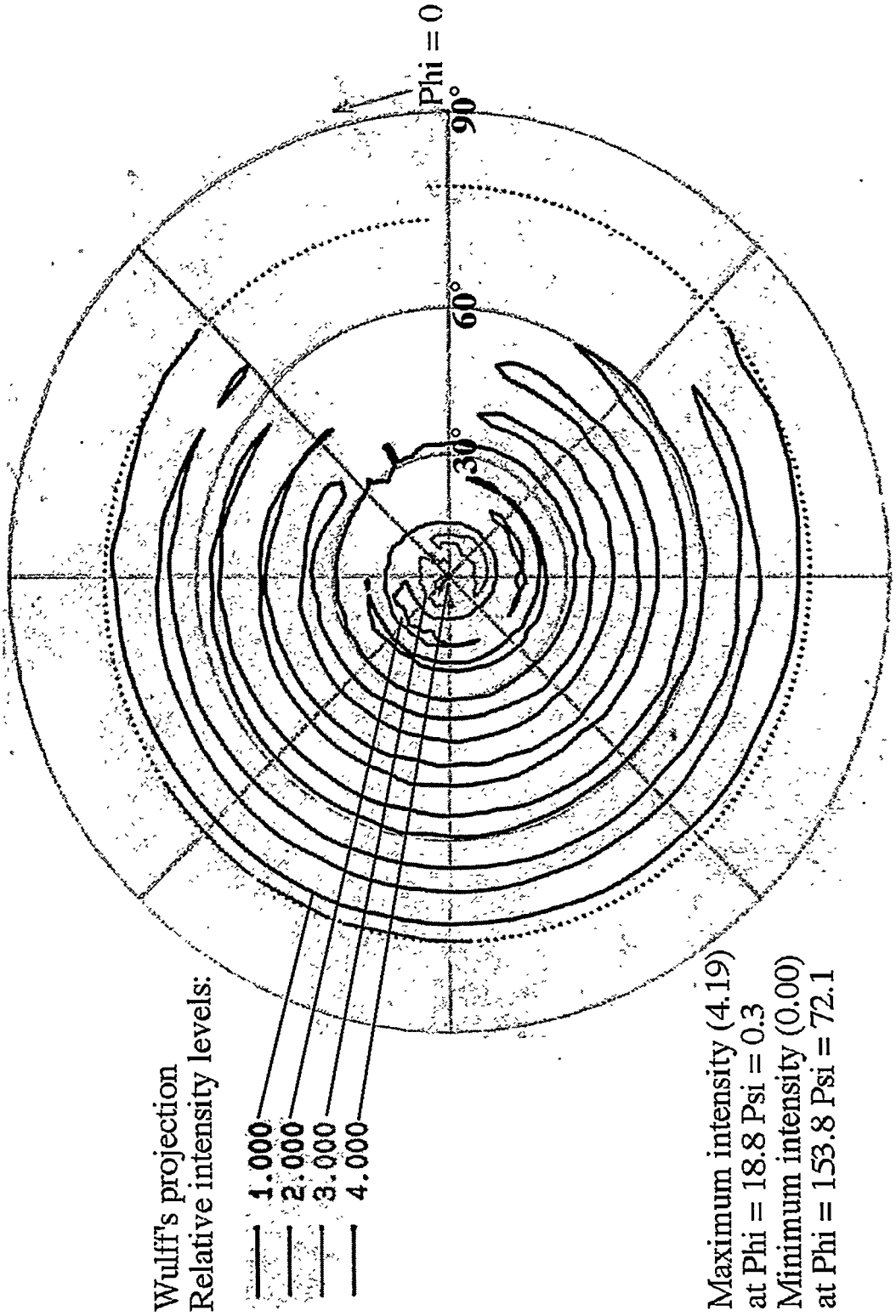
Phi = 0
90°
60°
30°
Wulff's projection
Relative intensity levels:
1.000
2.000
3.000
4.000
Maximum intensity (4.19)
at Phi = 18.8 Psi = 0.3
Minimum intensity (0.00)
at Phi = 153.8 Psi = 72.1

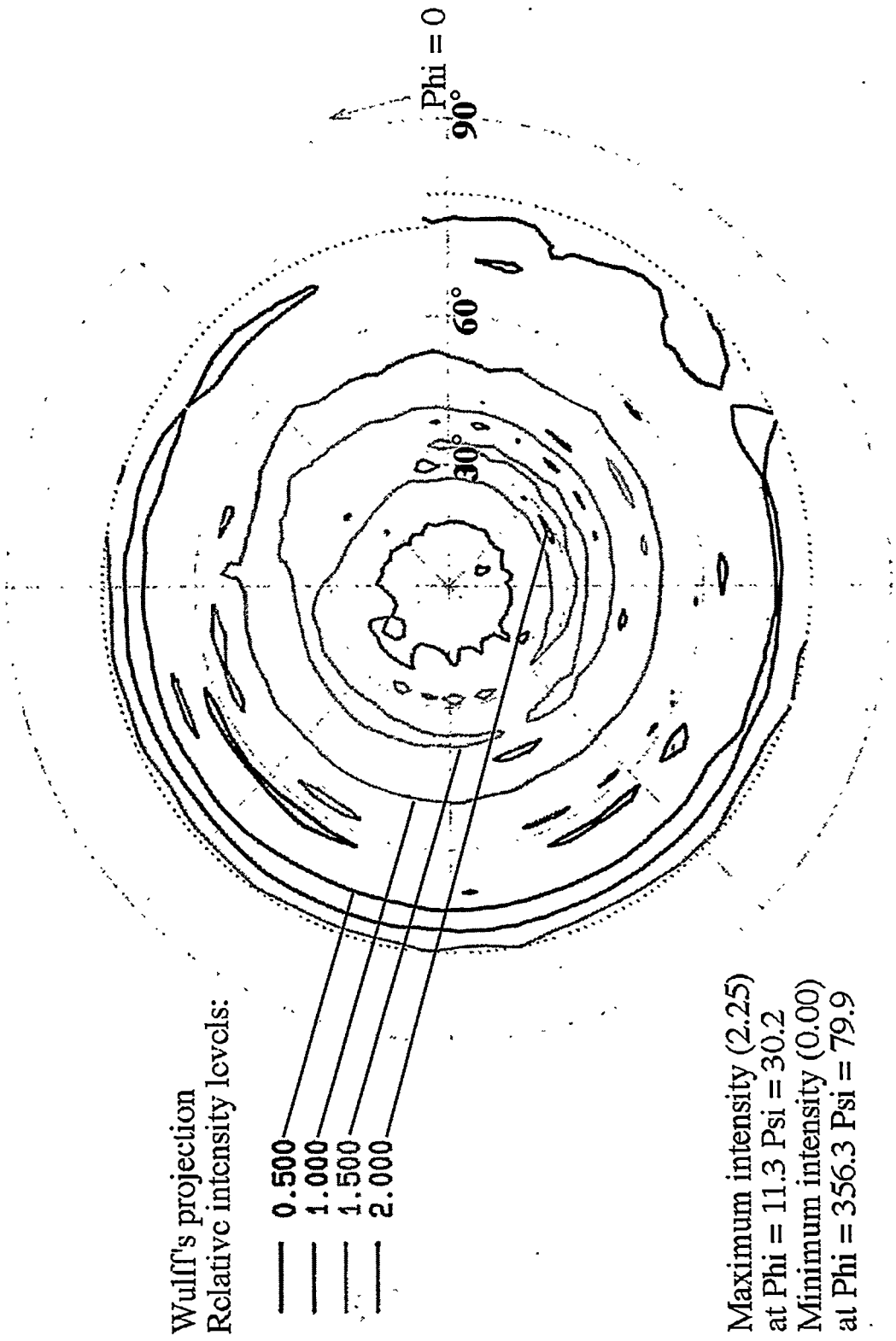
Phi = 0
90°
60°
30°
Wulff's projection
Relative intensity levels:
0.500
1.000
1.500
2.000
Maximum intensity (2.25)
at Phi = 11.3 Psi = 30.2
Minimum intensity (0.00)
at Phi = 356.3 Psi = 79.9

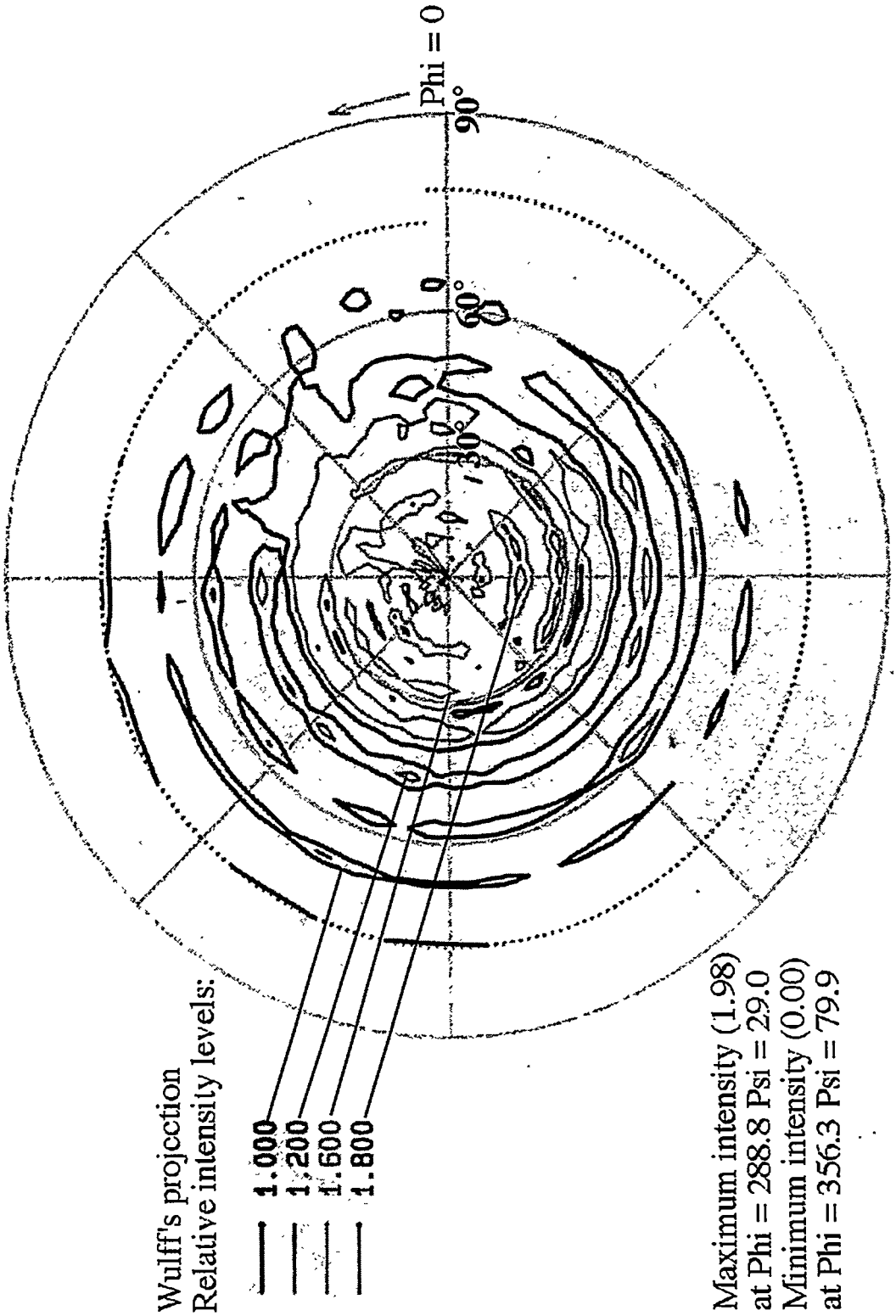
Phi = 0
90°
60°
30°
0
Wulff's projection
Relative intensity levels:
1.000
1.200
1.600
1.800
Maximum intensity (1.98)
at Phi = 288.8 Psi = 29.0
Minimum intensity (0.00)
at Phi = 356.3 Psi = 79.9

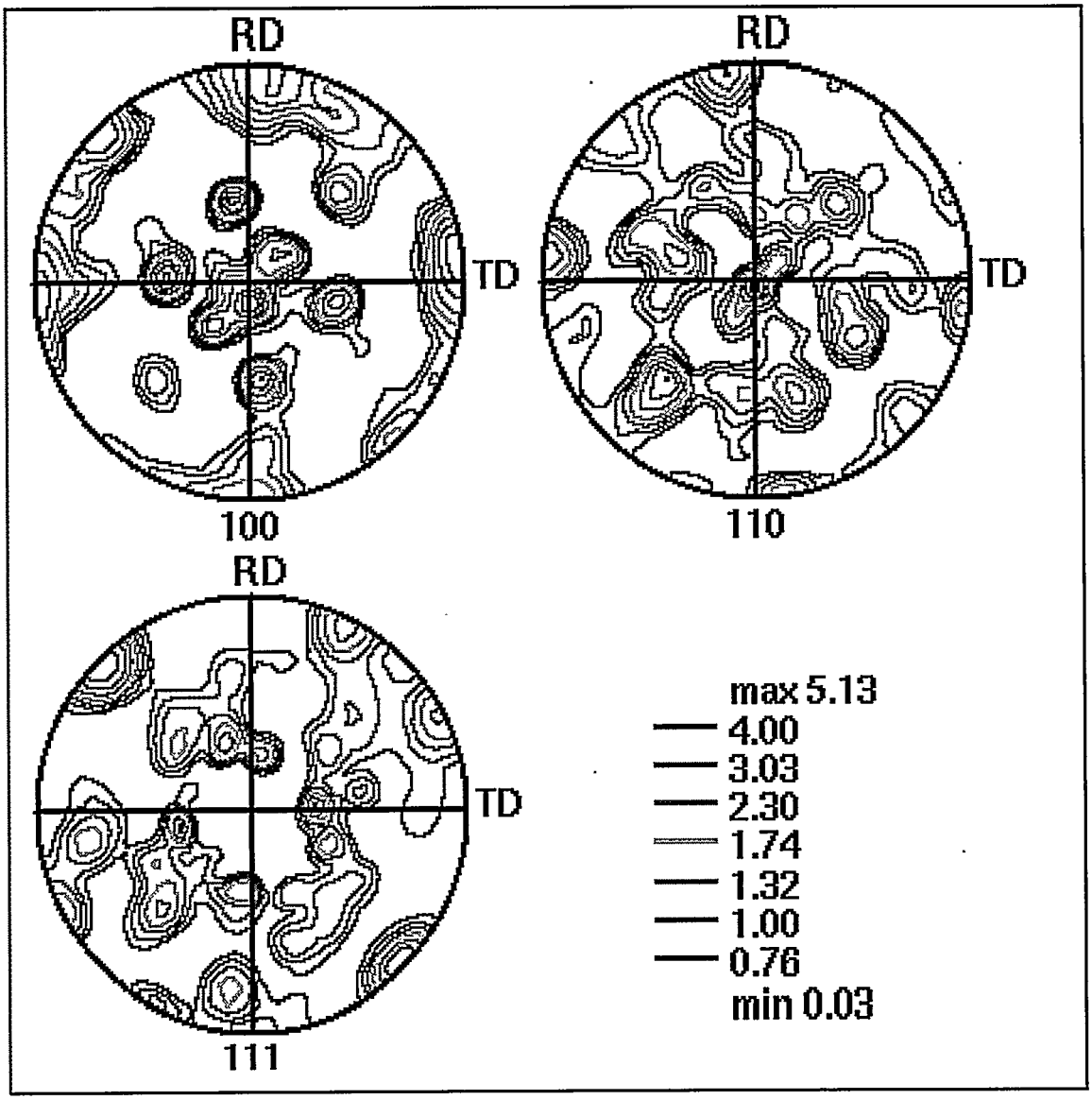

Figure 27 - FCC Al OIM pole figures for the Al_{GARS}-20Ti rod at $\eta = 2.5$ (transverse section). The rolling direction (RD) and transverse direction (TD) is irrelevant in these OIM images since the specimen is a rod (symmetrical around the transverse axis). The (100) plane shows a dual texture of <100> (strong central spot and spots at the poles) and <110> (four spots at Psi=45° and four along the edge). Similarly, the (110) plane shows the fiber axis orientations <100> and <110> as they would appear on a stereographic projection. (Although this is not the same as a stereographic projection. A stereographic projection is a map of directions and/or planes in one single crystal and a pole figure shows the distribution of a selected crystallographic plane relative to certain planes in the specimen.).

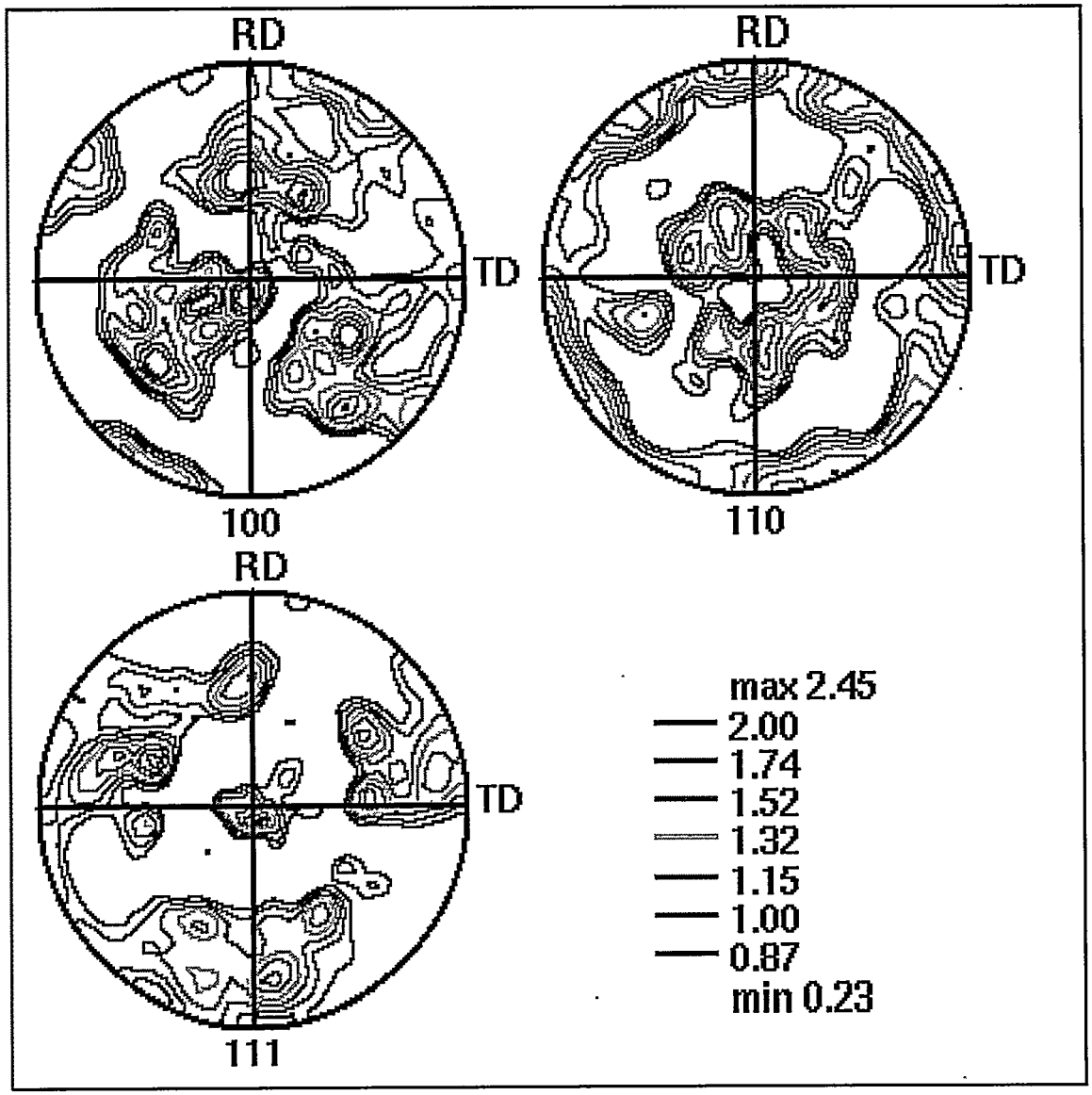

Figure 28 - FCC Al OIM pole figures for the Al_{GARS}-20Ti DMMC at $\eta = 2.5$. The rolling direction (RD) and transverse direction (TD) is irrelevant in these OIM images since the specimen is a rod (symmetrical around the transverse axis). The (100) plane shows a dual texture of <100> and <111> Similarly, the (111) plane shows the fiber axis orientations <100> and <111> as they would appear on a stereographic projection.

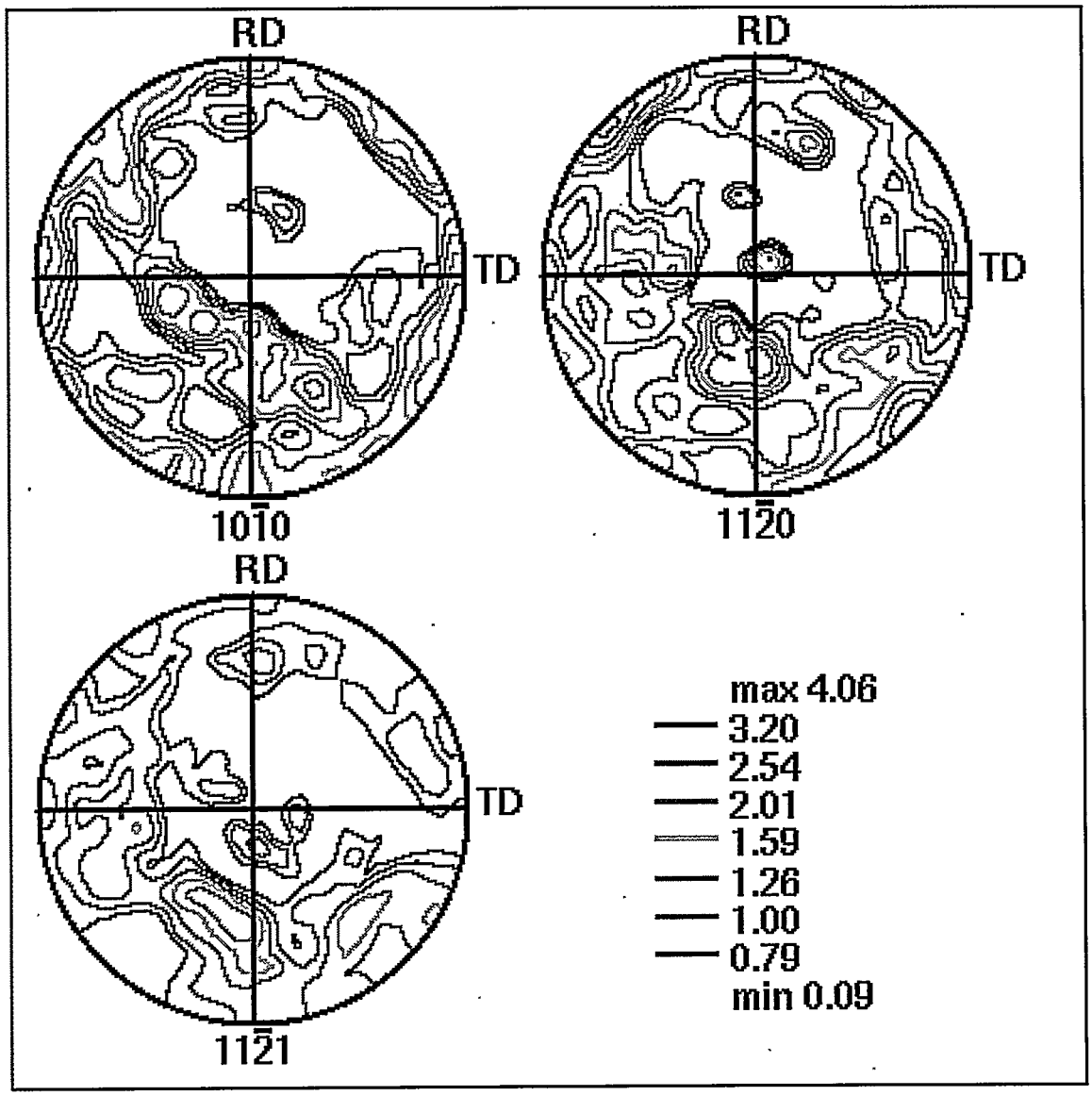

Figure 29 - HCP Ti OIM pole figures for Al_{GARS}-20Ti rod at $\eta = 2.5$ (transverse section) showing a $<11\bar{2}0>$ texture. The rolling direction (RD) and transverse direction (TD) is irrelevant in these OIM images since the specimen is a rod (symmetrical around the transverse axis).

4.3 Differential thermal analysis

DTA was done on the various deformation levels (η) to study the effect of deformation on the temperature of formation of Al_3Ti. The formation of Al_3Ti is an exothermic reaction, so it should show as a peak in a DTA curve. The failed 3rd extrusion was also analyzed and compared to a sample of approximately same η-value in an effort to explain what happened during the extrusion. (Figure 34)

The DTA measurements were done at a heating rate of 10°C/min. Results are given in Figures 30-34. The apparatus used had an unidentified background peak at about 220-290°C (See Figure 35), so the data from this temperature range are not reliable.
The results from Figures 30-33 are shown in Table 3 and Figures 36-37. The formation of Al_3Ti starts at lower temperature for higher η-values and smaller titanium filament thicknesses, as would be expected. At higher deformation, the stress in the sample increases. This results in a higher driving force for formation of Al_3Ti, so the intermetallic will form at a lower temperature as deformation increases. Previous investigations [32, 34] show that at higher deformation, the amount of dislocations increase up to a certain fiber thickness. An increasing amount of dislocations will give a decrease in the formation start temperature also, since dislocations may act as additional nucleation sites for Al_3Ti formation.

The failed η=10.3 sample showed no reaction during the heating cycle, as expected assuming that the sample reacted during the 3rd extrusion to form the intermetallic Al_3Ti. If the graph in Figure 36 is extrapolated down to $\eta \approx 13$ (The approximate η-value of the as-extruded sample), the temperature of reaction start would be 330°C. This is still higher than the temperature of the sample before extrusion (262°C), however, the extrusion itself generates so much heat that the temperature of the sample still can get high enough for Al_3Ti to form.

The temperature where the equilibrium (Al_3Ti) phase forms decreases with increasing deformation. This is presumably due to increased stress and dislocations in the sample. The failed 3rd extrusion does not show any reaction upon heating to 600°C, strengthening the suspicion that Al_3Ti already has formed. X-ray diffraction analysis was done on the samples to confirm the results predicted in DTA.

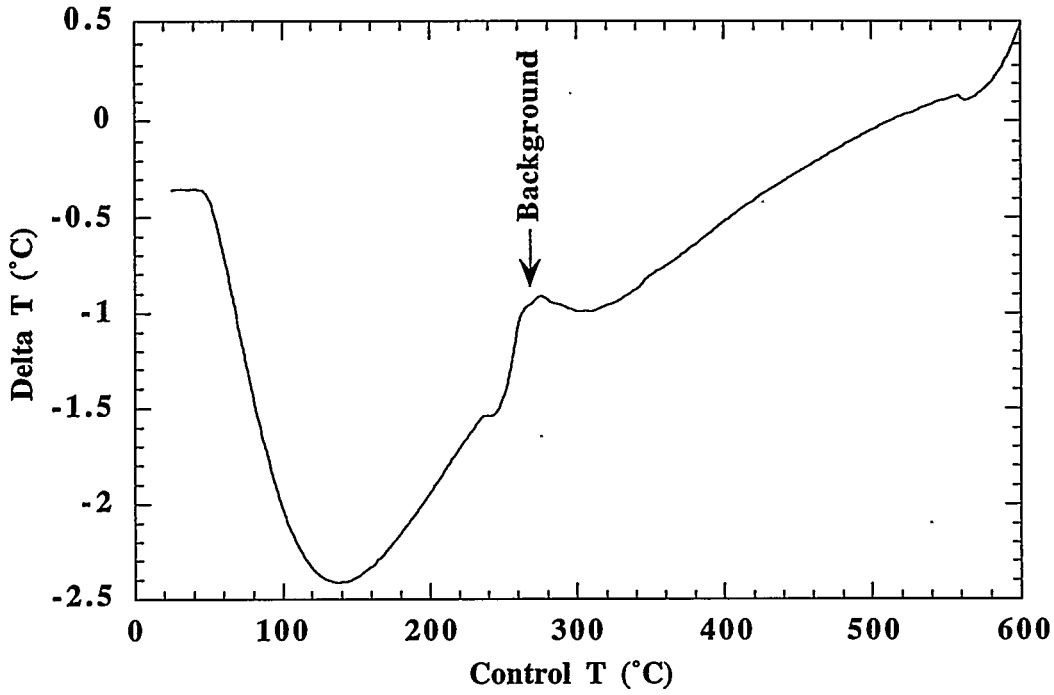

Figure 30 - DTA of Al_{GARS}-20Ti η=2.5 indicating a reaction start at about 550°C, presumably formation of the intermetallic Al_3Ti. The peak at 250°C is a background peak.

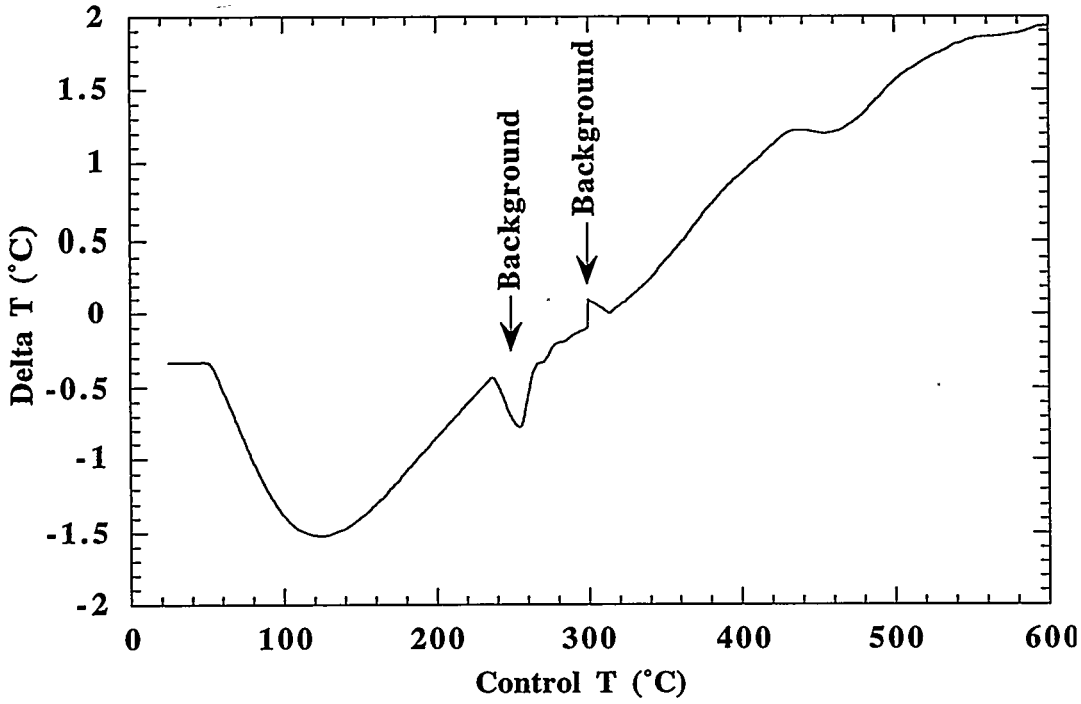

Figure 31 - DTA of Al_{GARS}-20Ti η=8.5 indicating a reaction start at about 420°C, presumably formation of the intermetallic Al_3Ti. The peak at 250°C is a background peak.

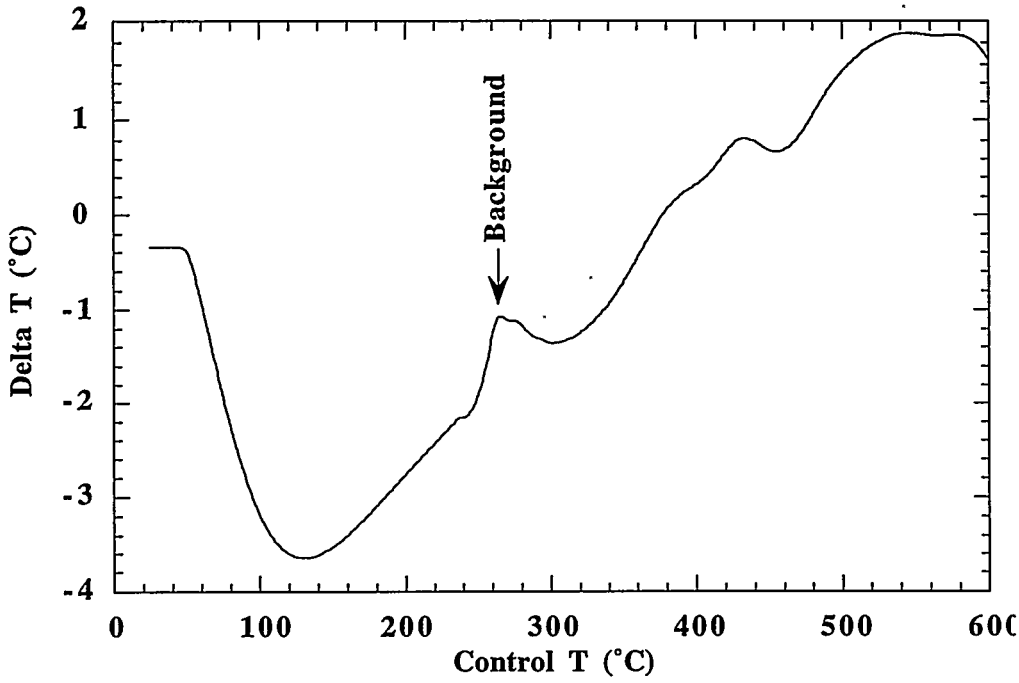

Figure 32 - DTA of Al_{GARS}-20Ti η=10.3 indicating a reaction start at about 390°C, presumably formation of the intermetallic Al_3Ti. The peak at 250°C is a background peak.

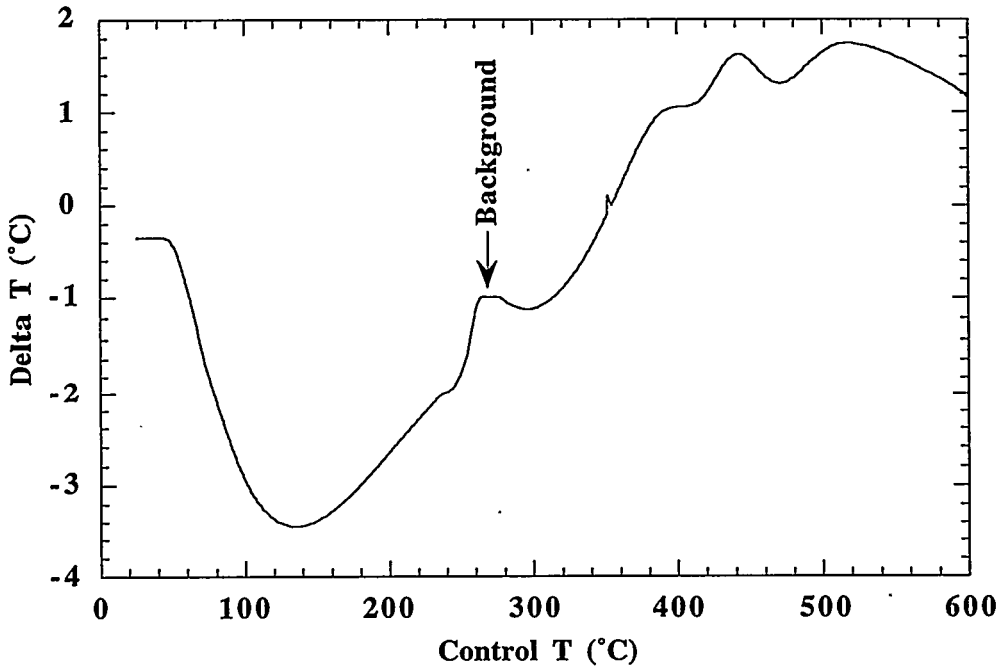

Figure 33 - DTA of Al_{GARS}-20Ti η = 12.1 indicating a reaction start at about 355°C, presumably formation of the intermetallic Al_3Ti. The peak at 250°C is a background peak.

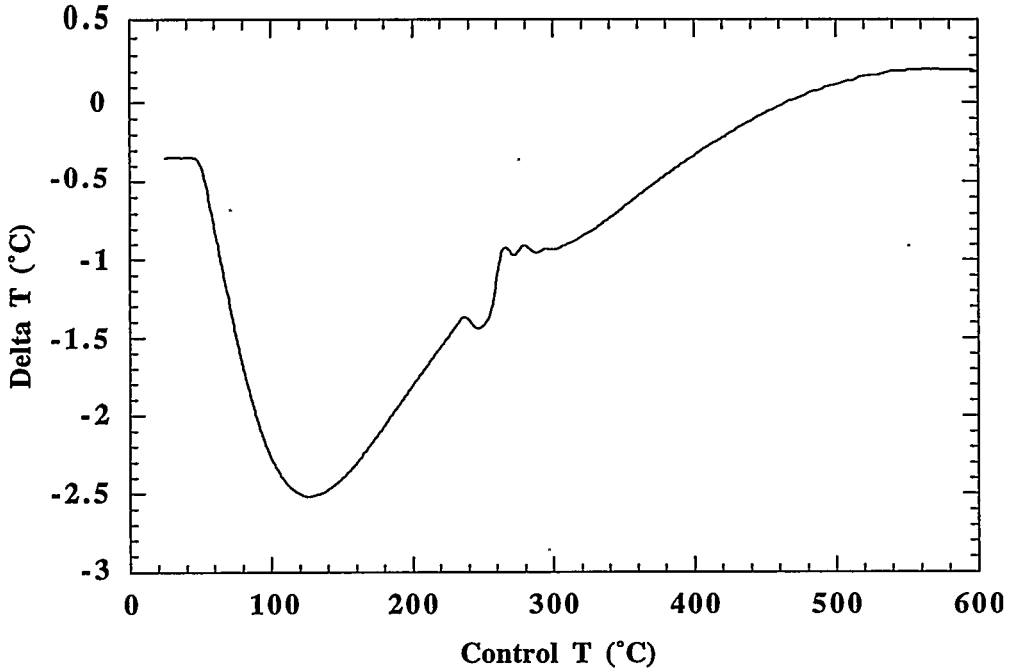

Figure 34 - DTA of Al_{GARS}-20Ti η=10.3, 3rd extrusion (failed). The peak seen in the η=10.3 sample before extrusion is absent in this graph, suggesting a reaction has occurred.

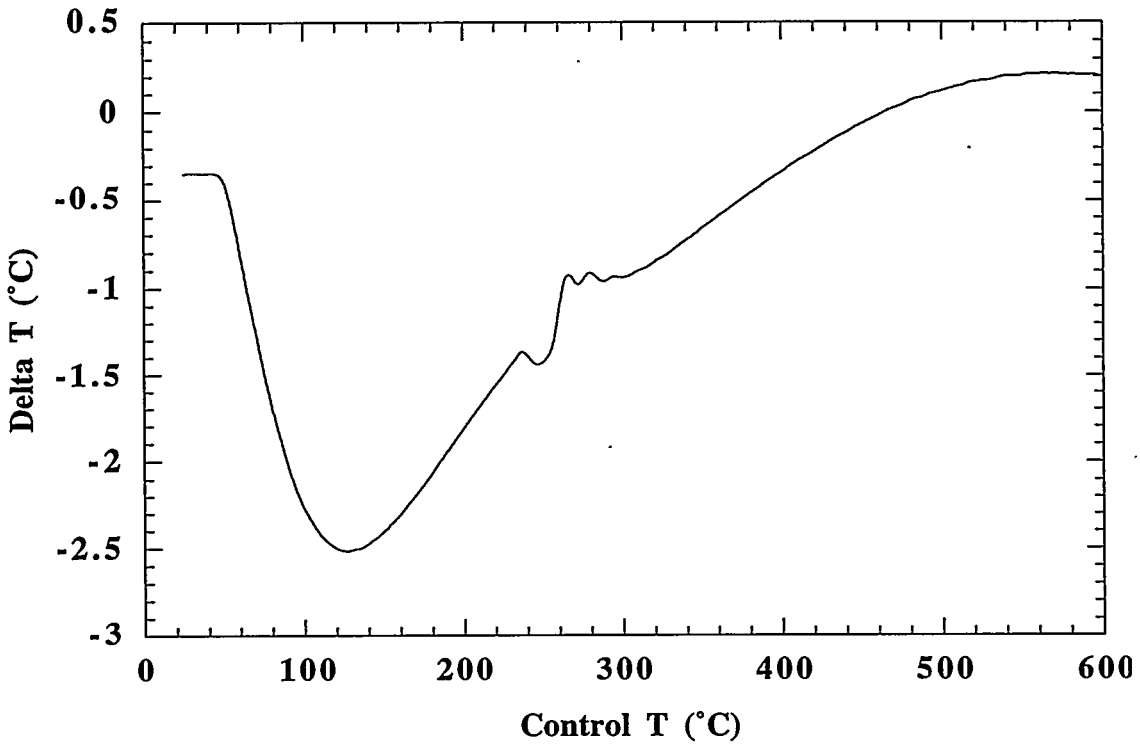

Figure 35 - DTA of an empty alumina crucible. The peak at about 250°C is the background peak mentioned in all the graphs above.

Table 3. Temperature of formation of Al_3Ti versus true strain for Al_{GARS}-20Ti.

Deformation true strain, η	Reaction start (approx.)
2.5	560°C
8.5	420°C
10.3	405°C
12.1	350°C

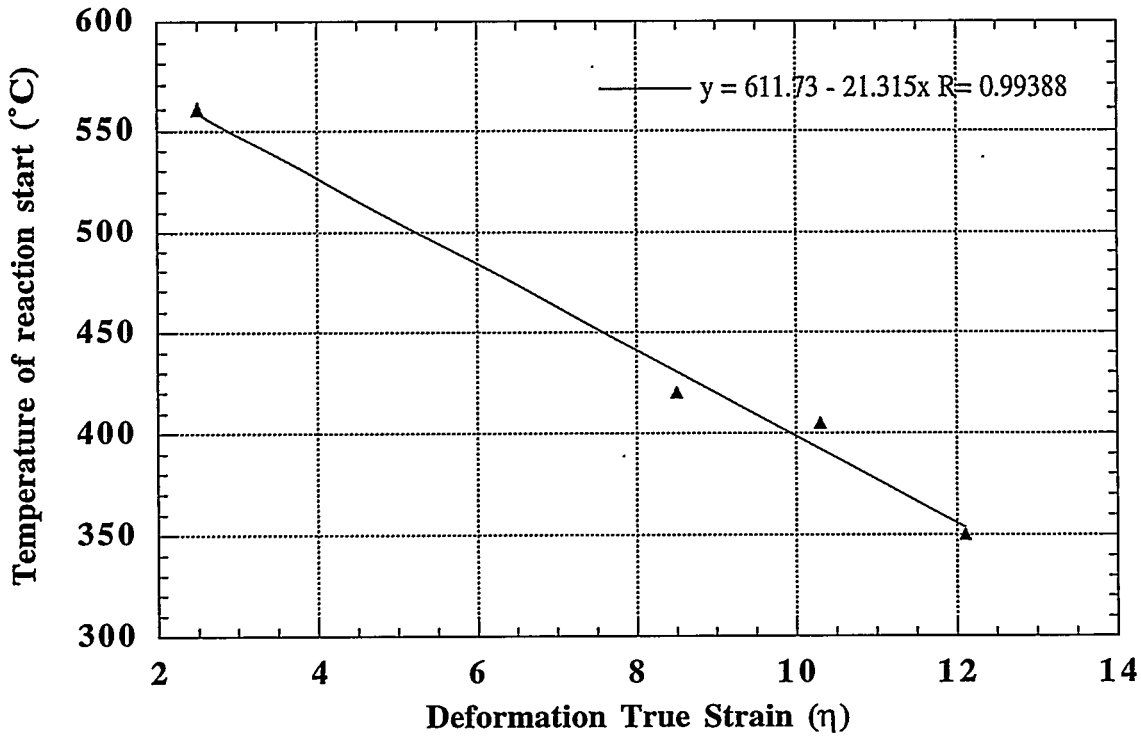

Figure 36 - The true strain dependence of the reaction start temperature for formation of Al_3Ti in Al_{GARS}-20Ti DMMC. The reaction start temperature decreases with increasing η and decreasing Ti filament thickness and spacing.

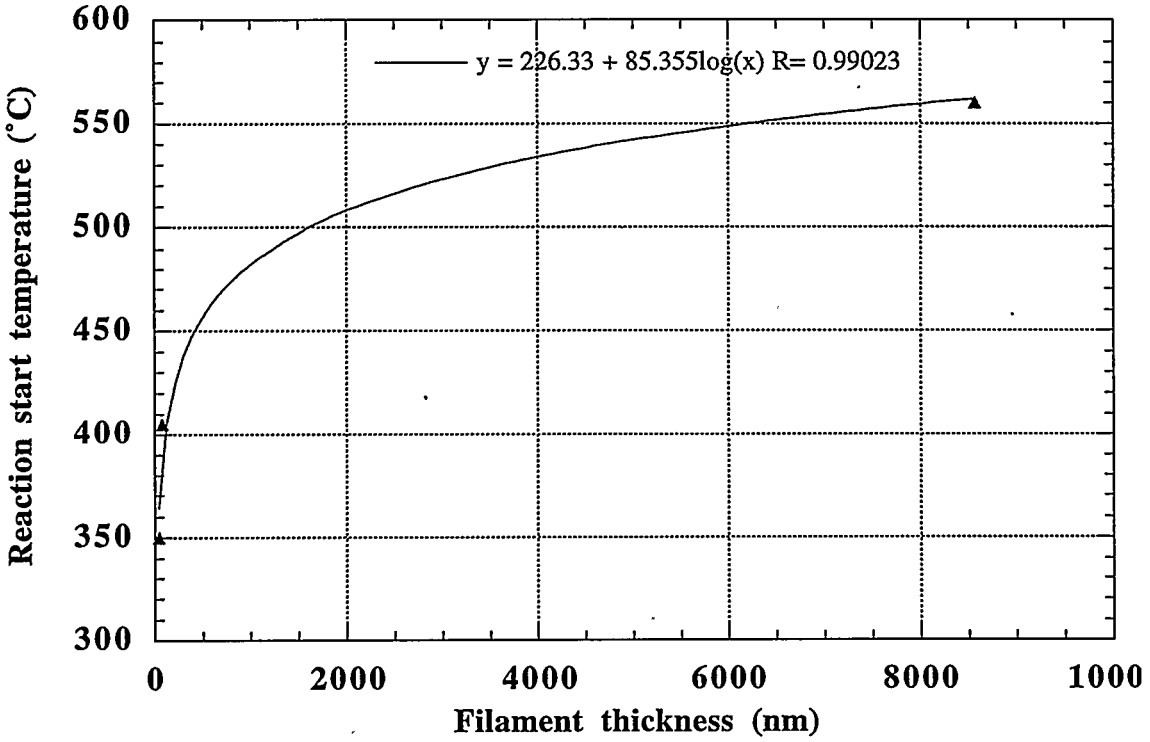

Figure 37 - The titanium filament thickness versus reaction start temperature for formation of Al_3Ti in Al_{GARS}-20Ti DMMC. The reaction start temperature increases logarithmic with titanium filament thickness and filament spacing.

4.4 X-ray diffraction analysis

The differential thermal analysis (DTA) gives an indication of the thermal reactions that occur in the samples during heating. The endproducts after the reaction are unknown. X-ray diffraction (XRD) analysis provides an easy and fast method to confirm the predicted endproducts in the DTA, and also to confirm what happened to the 3rd extrusion.

XRD analysis was performed on the pure starting powders (Figures 38-39) for reference. Analysis was also performed on the as-extruded (η=2.5) sample both before and after a heat treatment for 24 hours at 600°C to determine whether a reaction between the elements to form the equilibrium intermetallic Al_3Ti would occur (Figures 40-41). Lastly, analysis was done on the η=10.3 sample that failed during the 3rd extrusion to determine if formation of the brittle intermetallic Al_3Ti was what caused the failure (Figure 42).

The starting powders showed pure Al and pure Ti and no other elements present. The as extruded (η=2.5) sample showed a mixture of pure Al and pure Ti with no other phases, so in this sample no reaction has occurred between Ti and Al. The heat treated sample showed

a mixture of Al and Al_3Ti, as expected. This confirms that the reaction seen in the DTA curve (Figure 28) is a reaction between the pure elements to form Al_3Ti. Since there is no Ti left in the sample, the reaction is complete. The XRD pattern of the failed η=10.3 sample was similar to the XRD pattern of the η=2.5 heat treated sample; a mixture of the intermetallic Al_3Ti and pure Al. The 3rd extrusion failed due to the formation of the brittle equilibrium phase Al_3Ti.

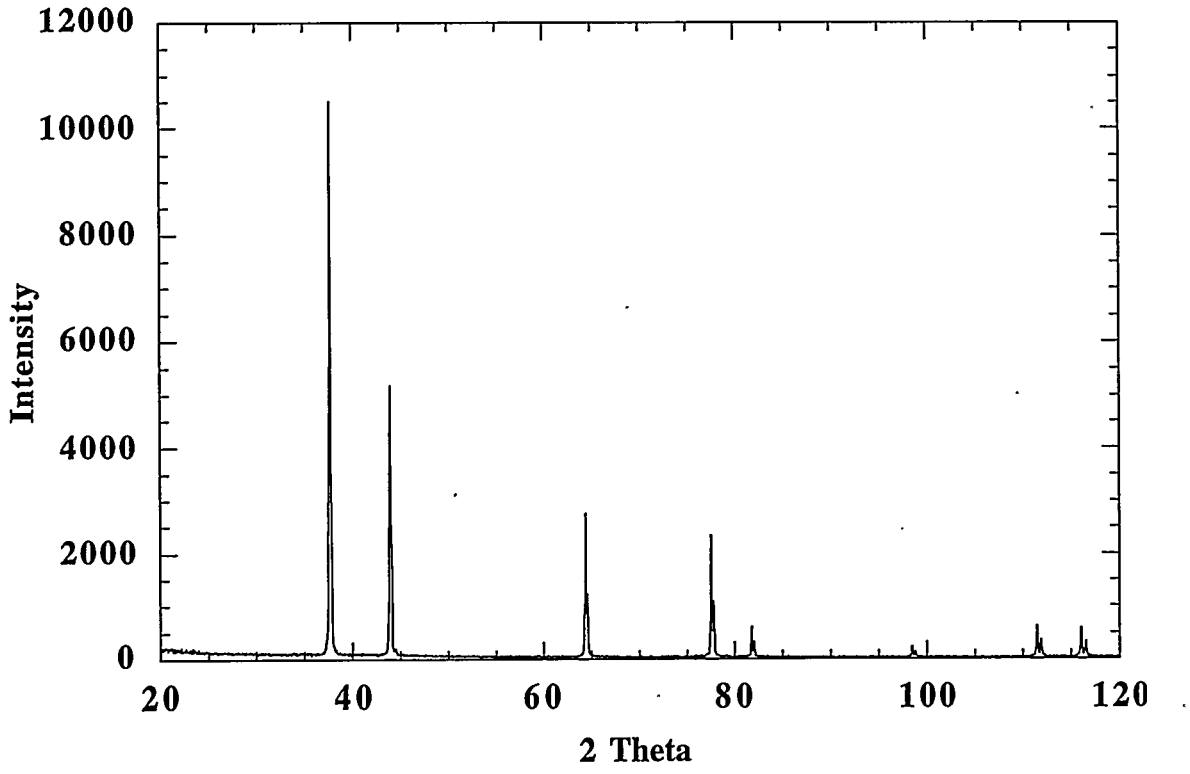

Figure 38 - XRD of Al powder. The pattern is consistent with what the expected for pure Al powder. Pure Al has high intensity peaks at the 2θ angles: 38.5°, 44.7°, 65.1° and 78.2°.

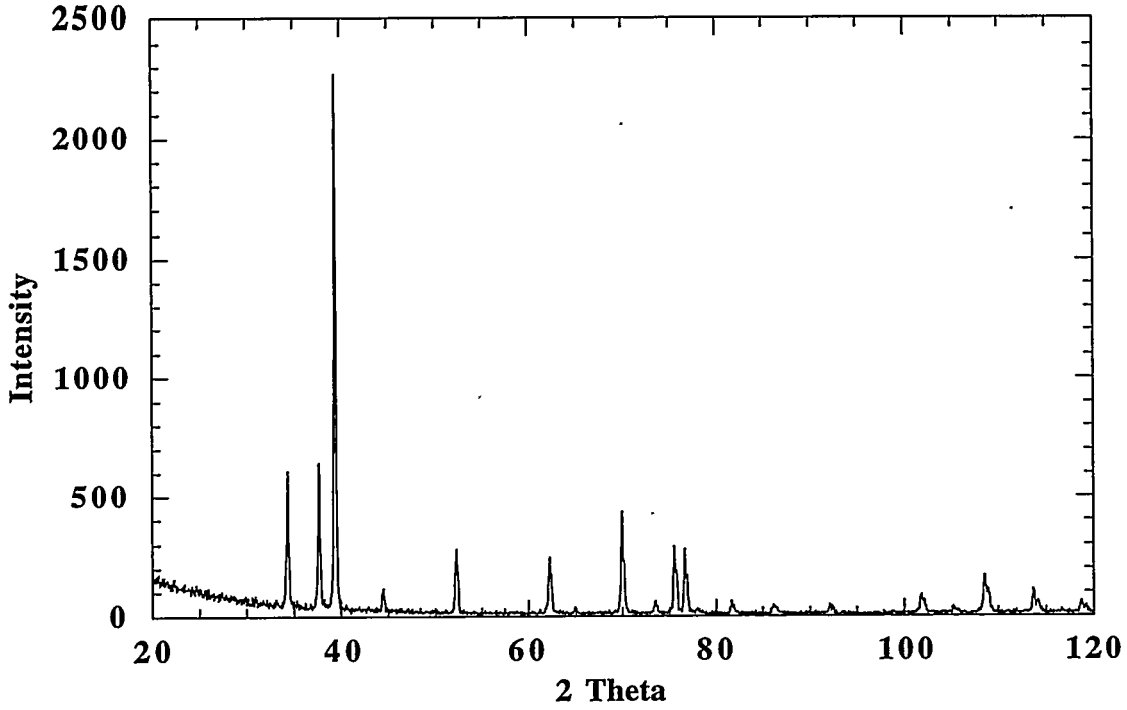

Figure 39 - XRD of Ti powder. The pattern fits the one of pure Ti. Pure Ti has high intensity peaks at the 2θ angles: 35.1°, 38.4°, 40.2°, 53.0°, 63.0°, 70.7° and 76.2°.

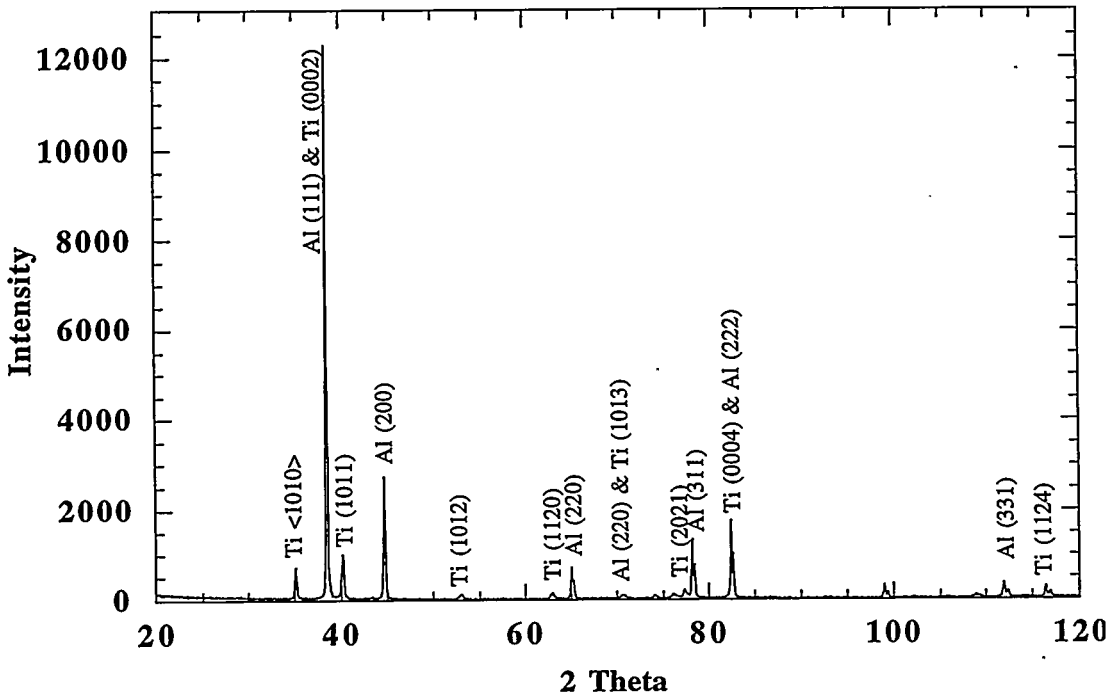

Figure 40 - XRD of η=2.5 before heat treatment. This pattern is consistent with the expected pattern; a mixture of Al and Ti with no intermetallics.

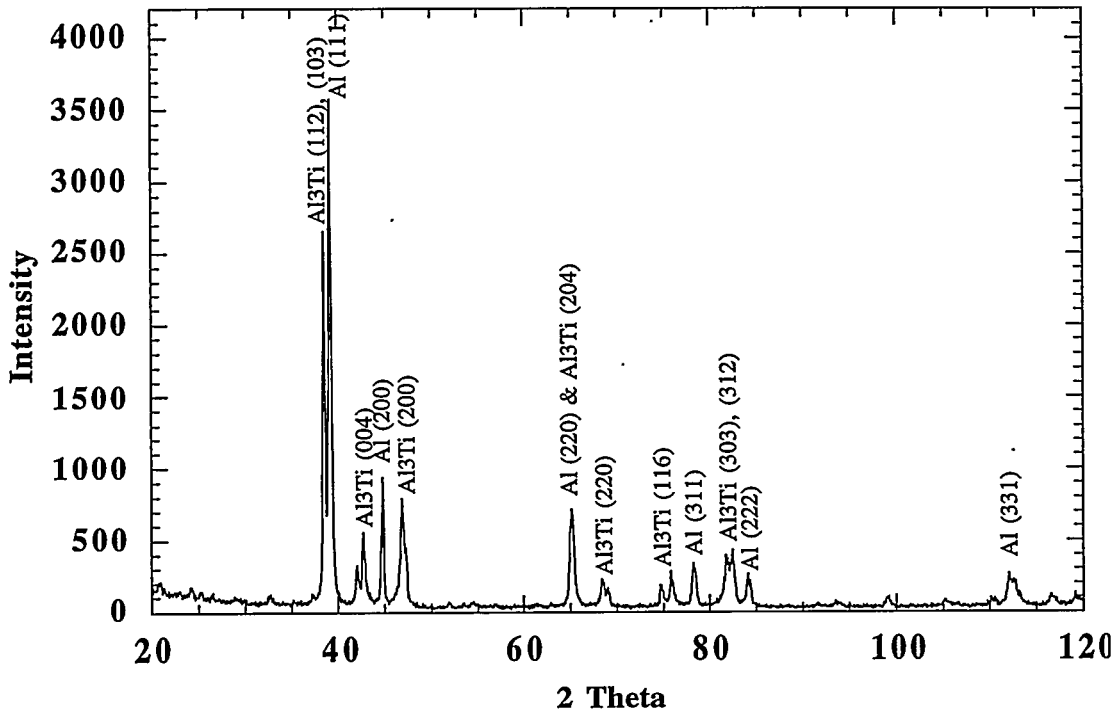

Figure 41 - XRD of η=2.5 heat treated for 24 hours at 600°C. The Al and Ti has reacted to form the intermetallic Al_3Ti. Excess Al is also left in the sample.

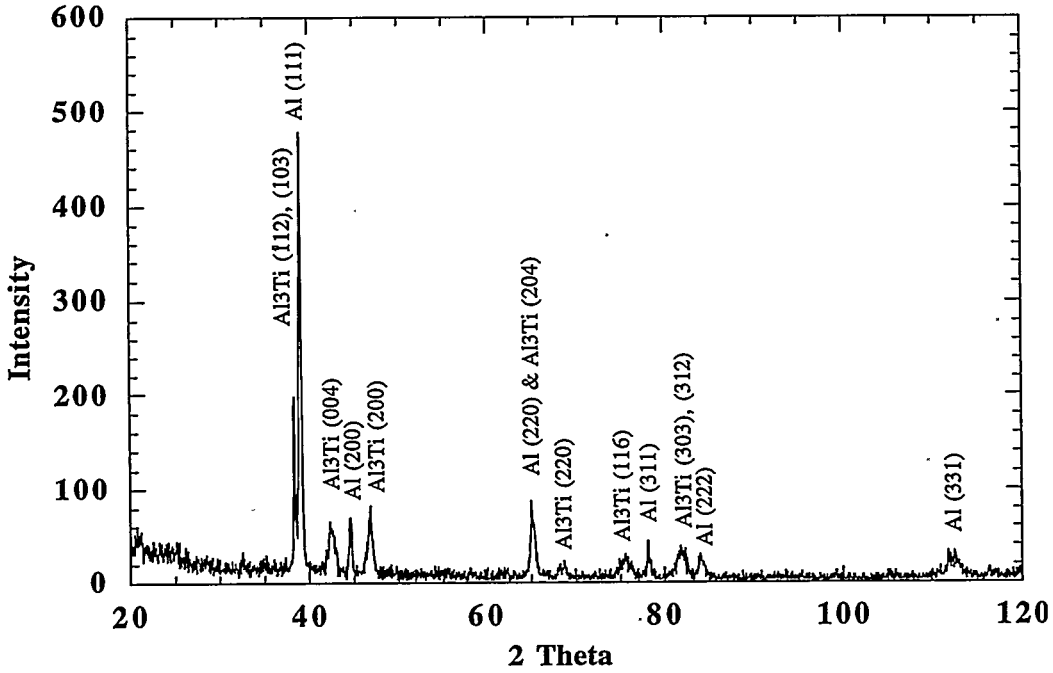

Figure 42 - XRD of the η=10.3 sample that failed during the 3rd extrusion. This pattern is identical to the XRD pattern of the heat treated η=2.5 sample (Figure 41); it contains the intermetallic Al_3Ti and pure Al.

4.5 Resistivity measurements

The objective of this study was to find a strong wire that could be used for high conductivity (or low resistivity) and high temperature applications. Study on the Cu-Cr system and other Cu-X systems [37, 48] shows that the conductivity decreases with strength (or η) (Figure 9). Kim et al [37] also discuss the effect of temperature on conductivity for an as-cast Cu-15 vol.% Cr alloy. As seen in Figure 8, the conductivity of this alloy decreases with increasing temperature. At the point where Cr precipitates, there is a slight increase in conductivity. Upon cooling and re-heating, the conductivity follows a path of higher conductivity due to this precipitation. Since the Al-20Ti alloy forms Al_3Ti upon heating, it is of interest to study the effect this formation will have on the resistivity based on the previously studied Cu-Cr and Cu-Nb systems. The highest η (12.1) had the highest strength and was therefore the only one studied. A closer look at the correspondence between temperature, true deformation strain and resistivity remains for future study.

Electrical resistivity, ρ, of the specimens at η=12.1 was measured at 300 K both before and after a 24 hour stress relief anneal at 200°C *in vacuo*, and the ultimate tensile strength of specimens at η=12.1 was also measured both before and after an 24 hour anneal at 200°C *in vacuo*. The annealing treatment had no significant effect on either strength or resistivity as shown in Table 4. A stress relief anneal would normally have no effect or a decreasing effect on the conductivity of a DMMC due to the decrease in dislocation density during the anneal.

Table 4. Electrical resistivity and ultimate tensile strength values for Al-20Ti at η = 12.1 before and after annealing 86,000 s (24 hours) at 473 K.

	Electrical resistivity, ρ ($n\Omega \cdot m$)	Ultimate tensile strength (MPa)
As-drawn (no anneal)	43	596 ± 10
After 200°C anneal	43	594 ± 17

Al_{GARS}-20Ti DMMC has the advantage that it has a high ratio of ultimate tensile strength to electrical resistivity (UTS:ρ). A survey of Al alloy properties in engineering handbooks [42] shows that Al alloy UTS:ρ ratios seldom exceed 10 MPa/$n\Omega \cdot m$, and the highest UTS:ρ ratio of any commercially available Al alloy is found in alloy 7049 in the T73 condition (UTS = 540 MPa, $\rho = 43$ $n\Omega \cdot m$). As Table 5 shows, the UTS:ρ ratio for both pre-annealed and post-annealed Al-20Ti DMMC's exceed this value.

Table 5 - Comparison of UTS:ρ ratios of the commercial alloy (7049, T73 condition) and pure aluminum with the highest ratio to Al_{GARS}-20Ti DMMC in two conditions.

Alloy	UTS:ρ ratio (MPa/nΩ·m)
Al_{GARS}-20Ti DMMC as drawn (η=12.1)	13.86
Al_{GARS}-20Ti DMMC with 24 hours, 200°C anneal (η=12.1)	13.81
Commercial alloy 7049, T73 condition	12.56
Pure Al, alloy 1100, O condition	3.10

Al_{GARS}-20Ti DMMC is expected to have a UTS:ρ ratio greater than a precipitation hardened Al alloy. The matrix of the DMMC is 99.99% purity Al filaments containing some fragments of Al_2O_3 but with no solid solution elements, GP zones, or other precipitates. The electrical resistivity of pure Ti is rather high for a metal (ρ=420 nΩ·m), but 80% of the cross sectional area of the DMMC is comprised of long strands of high-purity Al (ρ=26.5 nΩ·m at 300 K) which form a parallel conduction path with the Ti filaments. Since the strength of the Al_{GARS}-20Ti DMMC is due to the closely spaced Ti filaments in a pure Al matrix, it can conduct electricity with lower resistivity than is possible in a precipitation-hardened alloy. Due to the highly directional nature of the DMMC microstructure, the resistivity is probably anisotropic, and the resistivity in directions perpendicular to the specimen's rod axis (not measured in this study) is presumably higher than the values presented in Table 5. The contribution of the preferred orientations of the Al and Ti filaments to the electrical resistivity is assumed to be nil at 300 K, based on the findings of Hashimoto [43].

Electrical resistivity was also measured for the η=12.1 specimens as a function of heating and cooling (Figure 43). The sample was heated from room temperature to 500°C and cooled back down to room temperature again. The inflection point at ≈340°C correspond to the peak found in DTA at 350°C (η=12.1) where Al_3Ti forms from the pure elements. Similarly to the Cu-Cr [37], the resistivity change permanently when Al_3Ti forms. Upon cooling, the resistivity never goes back to the initial value.

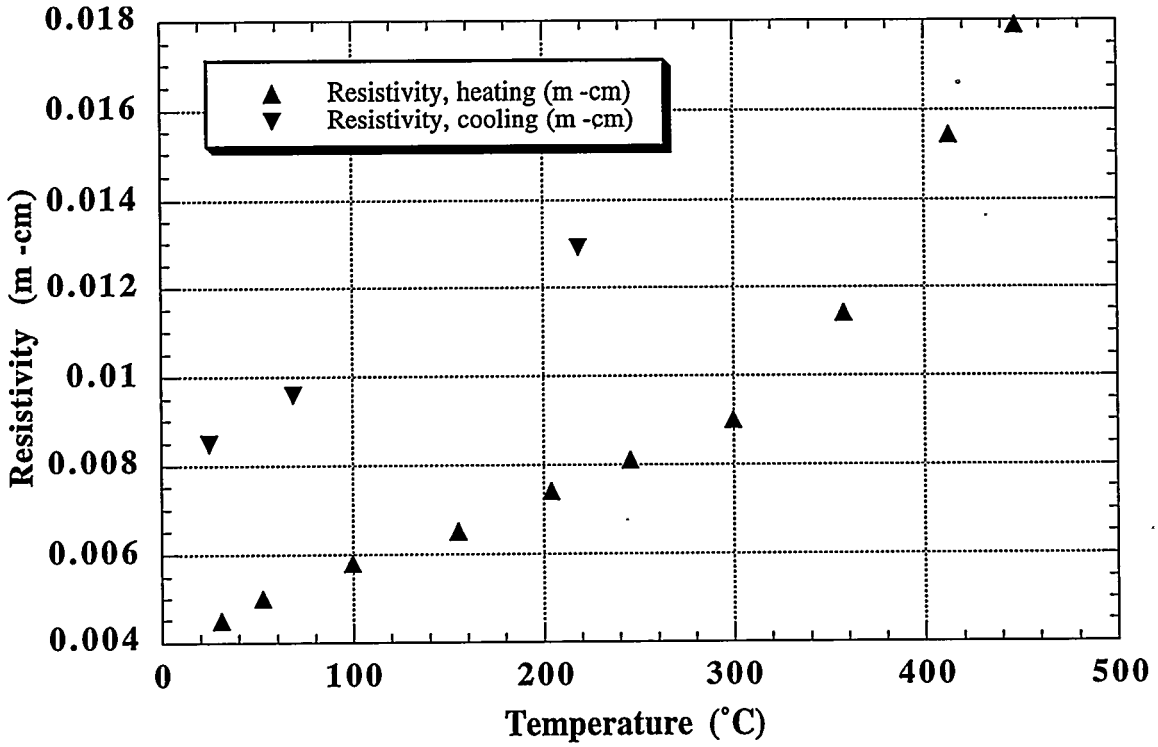

Figure 43 - A plot of resistivity of a pure Al-20Ti specimen at $\eta = 12.1$ during a heating cycle of 0.055 °C per second followed by cooling to room temperature. The inflection point at 340°C in the heating curve is thought to correspond to the reaction to form Al_3Ti from the pure metallic elements.

4.6 Microscopy results

4.6.1 SEM results

Microstructure is closely related to the strength of an axisymmetrically deformed material. An optical microscope has a too poor resolution for the Al-20Ti alloy, so SEM was used in order to study the morphology and to see how the thickness and spacing of the filaments affected the strength of the material.

SEM samples of the various deformation true strains were prepared. No etchant was used as the Al and Ti are far enough apart in atomic number to provide a good atomic number contrast in the back scattered electron (BSE) image mode on the microscope. For most of the samples, both longitudinal and transverse SEM samples were made. (See Figure 44.)

The classic "convoluted ribbon shaped" filaments seen in Figures 44-49 is to be expected from the $\langle 10\bar{1}0 \rangle$ fiber axis orientation assumed by axisymmetrically deformed Ti.

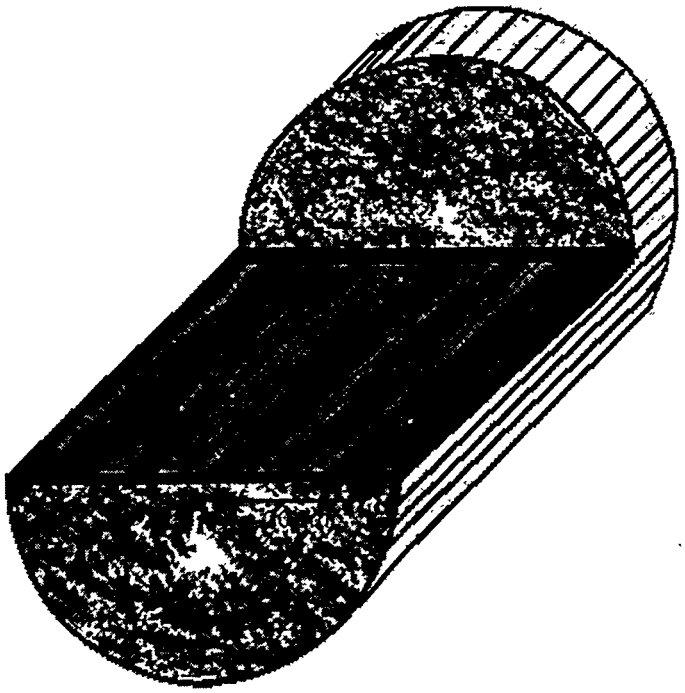

Figure 44 - Pictorial depiction of transverse and longitudinal SEM micrographs of pure Al-20Ti deformation processed to a true strain (η) of 10.3

This filament shape is quite similar to the BCC Nb second phase filaments observed in Al-Nb DMMC's [11, 12] and by several investigators [1-10] in Cu-Nb DMMC's. It is also similar to the filament shape observed in HCP Ti and HCP Y in Ti-Y DMMC's [15]. After the first extrusion (Figure 49A), there is a small amount of deformation of the Ti-particles. A few elongated filaments can be observed even in the transverse direction. After some swaging of this sample (Figure 49B), the convoluted ribbon shaped filaments are much more pronounced. And at η=12.1, there are no spherical particles left. All of the sample consists of closely spaced, elongated filaments. This change in the shape and spacing of the filaments is a possible explanation for the increase in strength with deformation, and will be discussed further in a later chapter.

Although the bulk of the DMMCs consist of kinked, ribbon shaped titanium filaments, a significant change in microstructure is observed towards the edge of the samples (Figure 50). The edge has a microstructure more typically seen in rolled sheets. This change in microstructure is thought to be the reason for the change in texture seen in the OIM analysis.

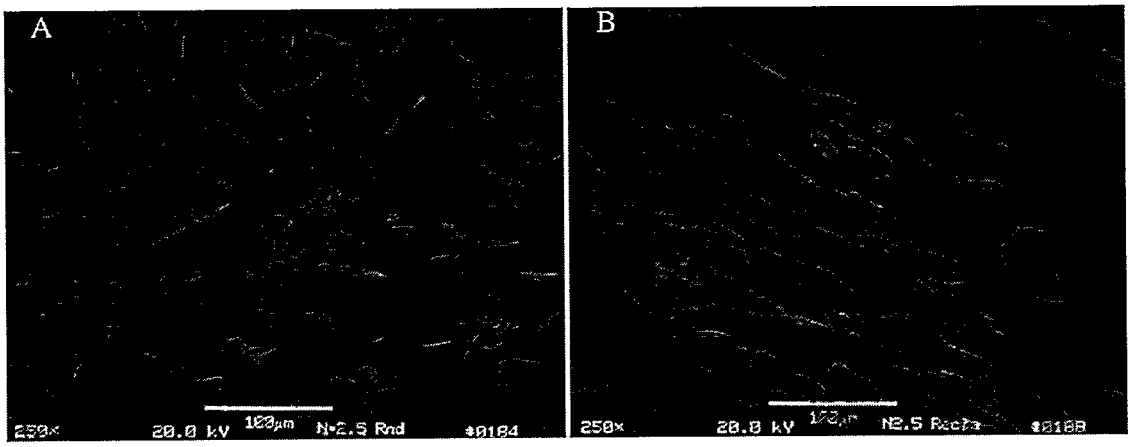

Figure 45- SEM micrograph of Al_{GARS}-20Ti deformation processed to a true strain (η) of 2.5 and mounted in transverse section, 45A at left (specimen rod axis normal to the plane of the micrograph) and mounted in longitudinal section, 45B at right (specimen rod axis parallel to the plane of the micrograph). The Al is dark gray, and the Ti is light gray in these back-scattered electron images.

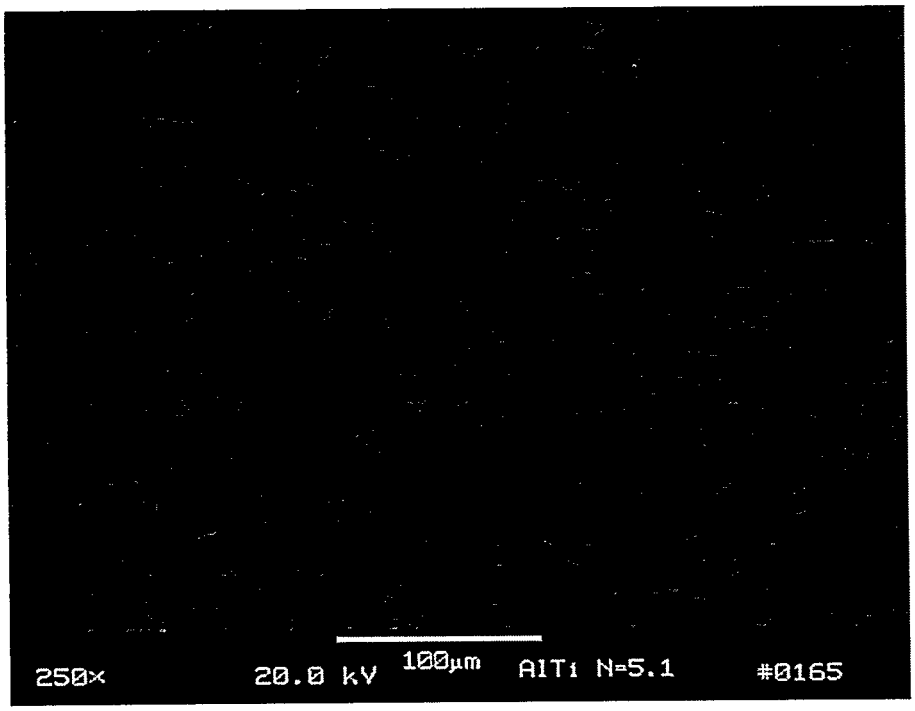

Figure 46 - SEM micrograph of Al_{GARS}-20Ti deformation processed to a true strain (η) of 5.1 and mounted in transverse section (specimen rod axis parallel to the plane of the micrograph). The Al is dark gray, and the Ti is light gray in these back-scattered electron images.

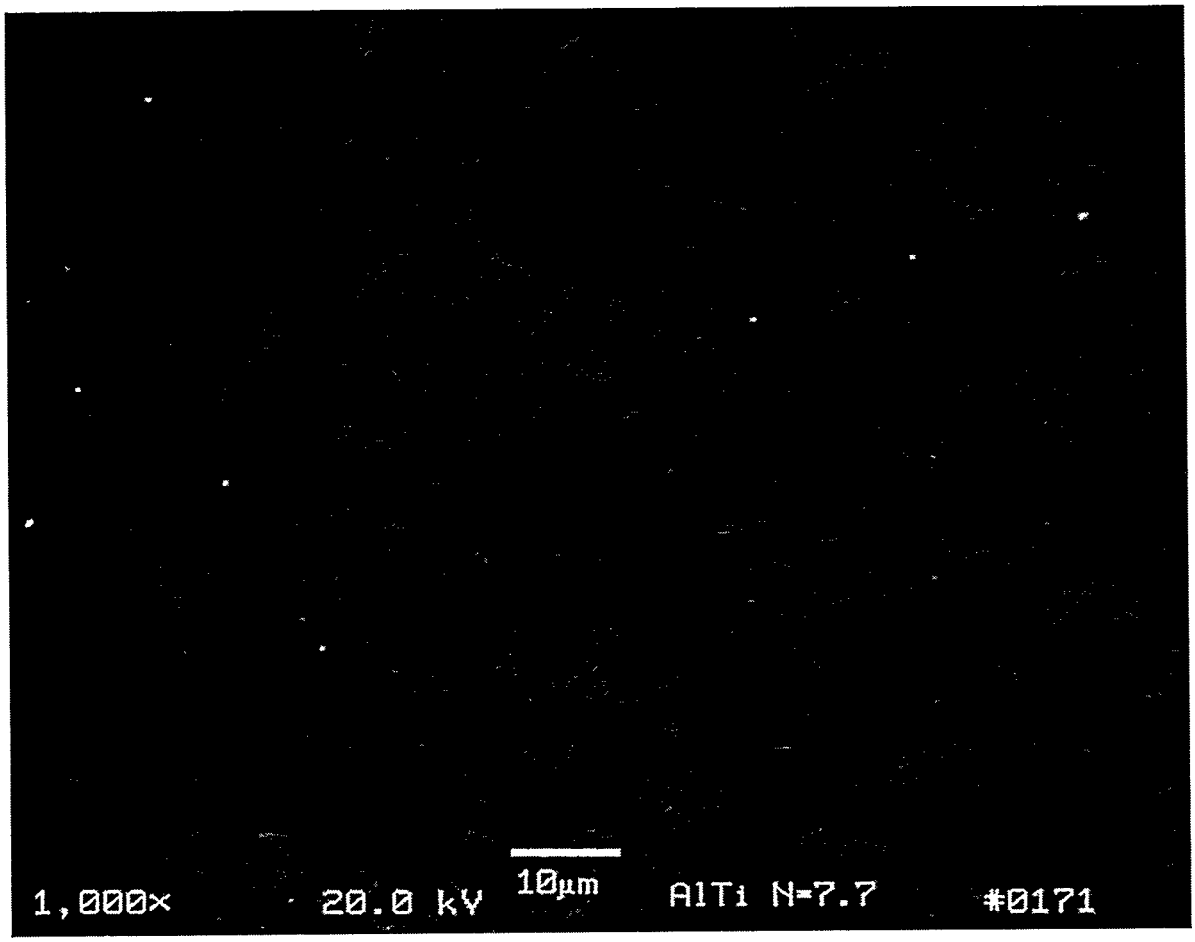

Figure 47 - SEM micrograph of pure Al-20Ti deformation processed to a true strain (η) of 7.7 and mounted in transverse section.

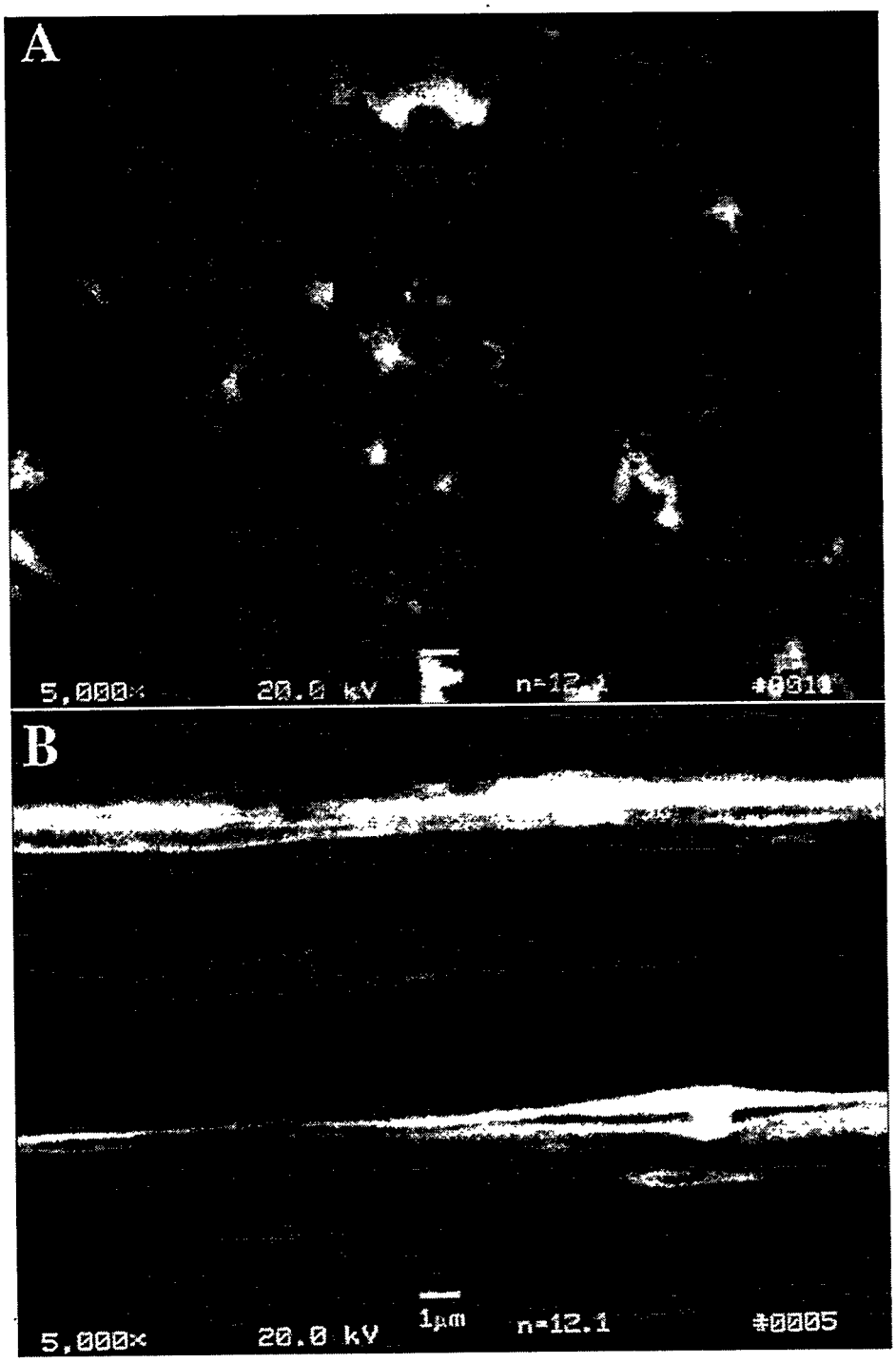

Figure 48 - SEM micrograph of Al_{GARS}-20Ti deformation processed to a true strain (η) of 12.1 and mounted in transverse section (specimen rod axis normal to the plane of the micrograph) in A, top, and mounted in longitudinal section (specimen rod axis parallel to the plane of the micrograph) in B, bottom. The Al is dark gray, and the Ti is light gray in this back-scattered electron image.

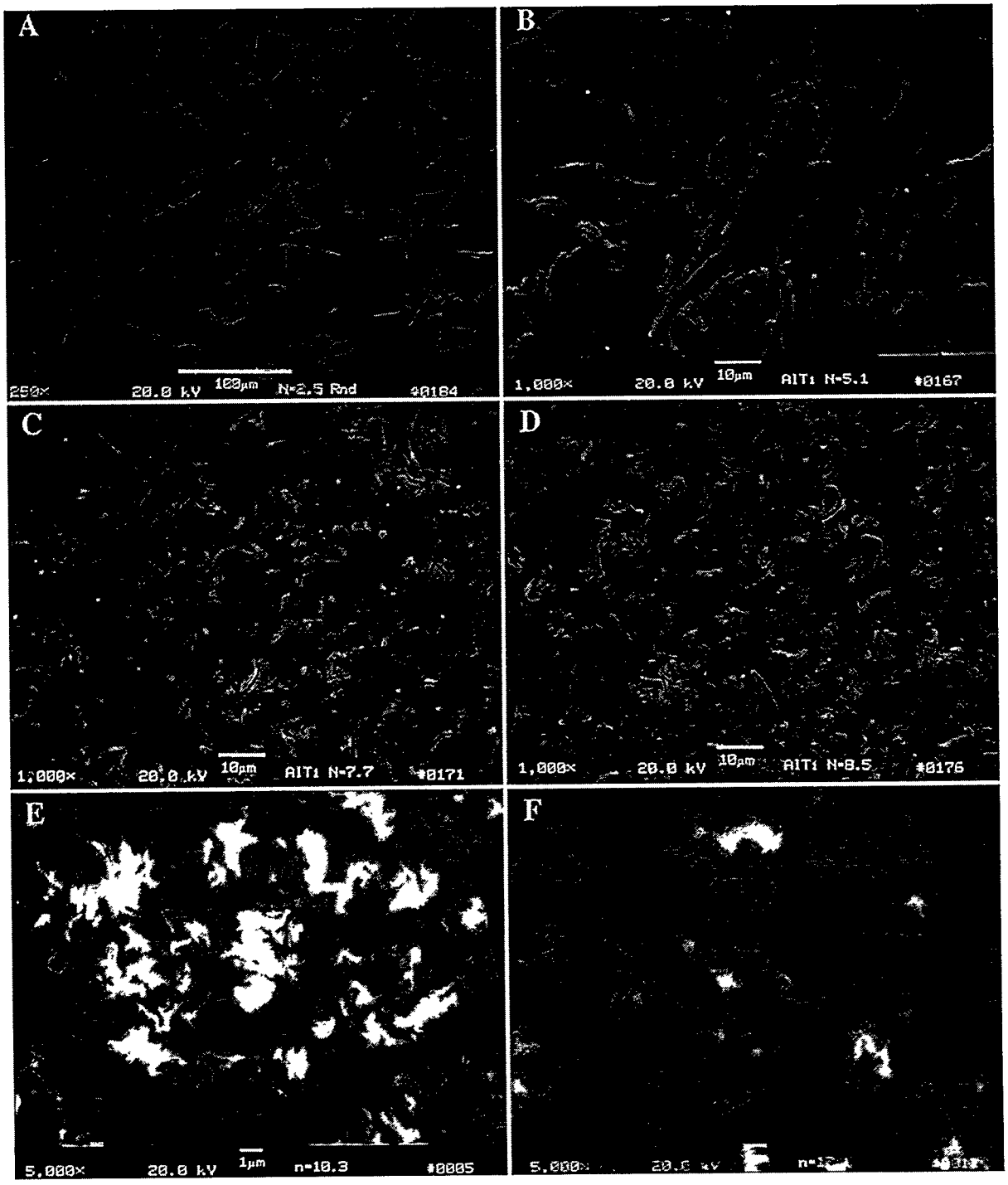

Figure 49 - SEM image of Al_{GARS}-20Ti at the various stages of deformation: 49A - as extruded first time ($\eta = 2.5$), 49B - extruded once, swaged some ($\eta = 5.1$), 49C - as extruded 2nd time ($\eta = 7.7$), 49D - extruded twice, swaged some ($\eta = 8.5$), 49E - extruded twice, swaged some ($\eta = 10.3$), 49F - extruded twice, swaged some, wire drawn ($\eta = 12.1$). 49 E&F are taken at 2500x, the rest of the micrographs are taken at 1000x.

Figure 50 - Change in microstructure from the edge of an Al-20Ti DMMC (η=7.7), left, and the bulk of the axisymmetrically deformed sample, right. The edge has a microstructure commonly seen in rolled sheet, while the bulk has the typical microstructure of a rod.

4.6.2 TEM results

The microstructure of the DMMCs is one of the main reasons for the high strength observed in this type of materials. The classical kinked, ribbon shaped filaments act as barriers to dislocation movement, and strengthen the material. SEM study give a good indication of the microstructure, but the resolution limitations of the SEM make it difficult to see some of the finest filaments. TEM provides a better resolution and a chance to study the formation of dislocations within the sample.

The highest η (10.3 and 12.1) samples were studied in the TEM. The samples were cut into 3 mm discs, approx. 0.1 mm thick, polished down and ion milled in a Gatan Ion Miller model 600 at a voltage of 5 V and 5 mA current through each of the two ion guns. The highest η (12.1) was too small to cut a 3 mm diameter disc, so the wire was cut into 4 small pieces and bundled up inside a small stainless steel tube. Epoxy was used to glue the pieces together before transverse discs were cut from the bundled sample and prepared as described above.

An extensive study of the dislocations was beyond the scope of this study. The main purpose for the TEM analysis was to see if the dislocations strengthened the material, to have a look at the microstructure, and to gain information about the filament thickness and spacing beyond the resolution of the SEM.

The TEM images show the classical kinked Ti-filaments (Figures 51-54) for both the 10.3 and the 12.1 sample. All images are of the transverse direction, and the dark filaments are Ti-filaments. Both samples contain many dislocations, a possible cause for the strengthening during deformation. The filament thickness and spacing decrease with deformation, as will be discussed later.

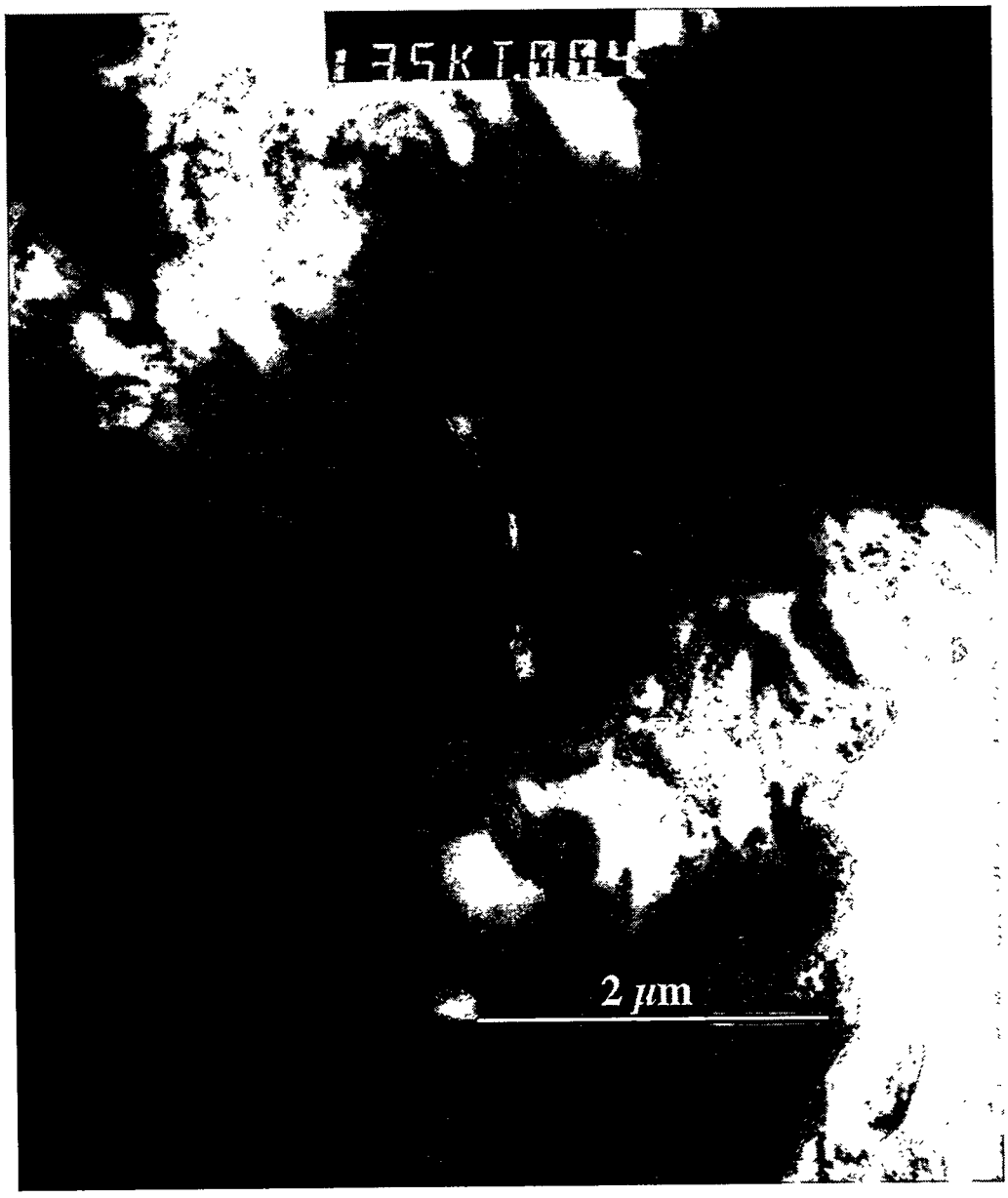

Figure 51 - TEM micrograph of pure Al-20Ti deformation processed to a true strain (η) of 10.3 and mounted in transverse section (specimen rod axis normal to the plane of the micrograph).

Figure 52 - Bright Field TEM micrograph of Al_{GARS}-20Ti deformation processed to a true strain (η) of 10.3 and mounted in transverse section (specimen rod axis normal to the plane of the micrograph).

Figure 53 - Bright field TEM micrograph of Al_{GARS}-20Ti deformation processed to a true strain (η) of 10.3 and mounted in transverse section (specimen rod axis normal to the plane of the micrograph).

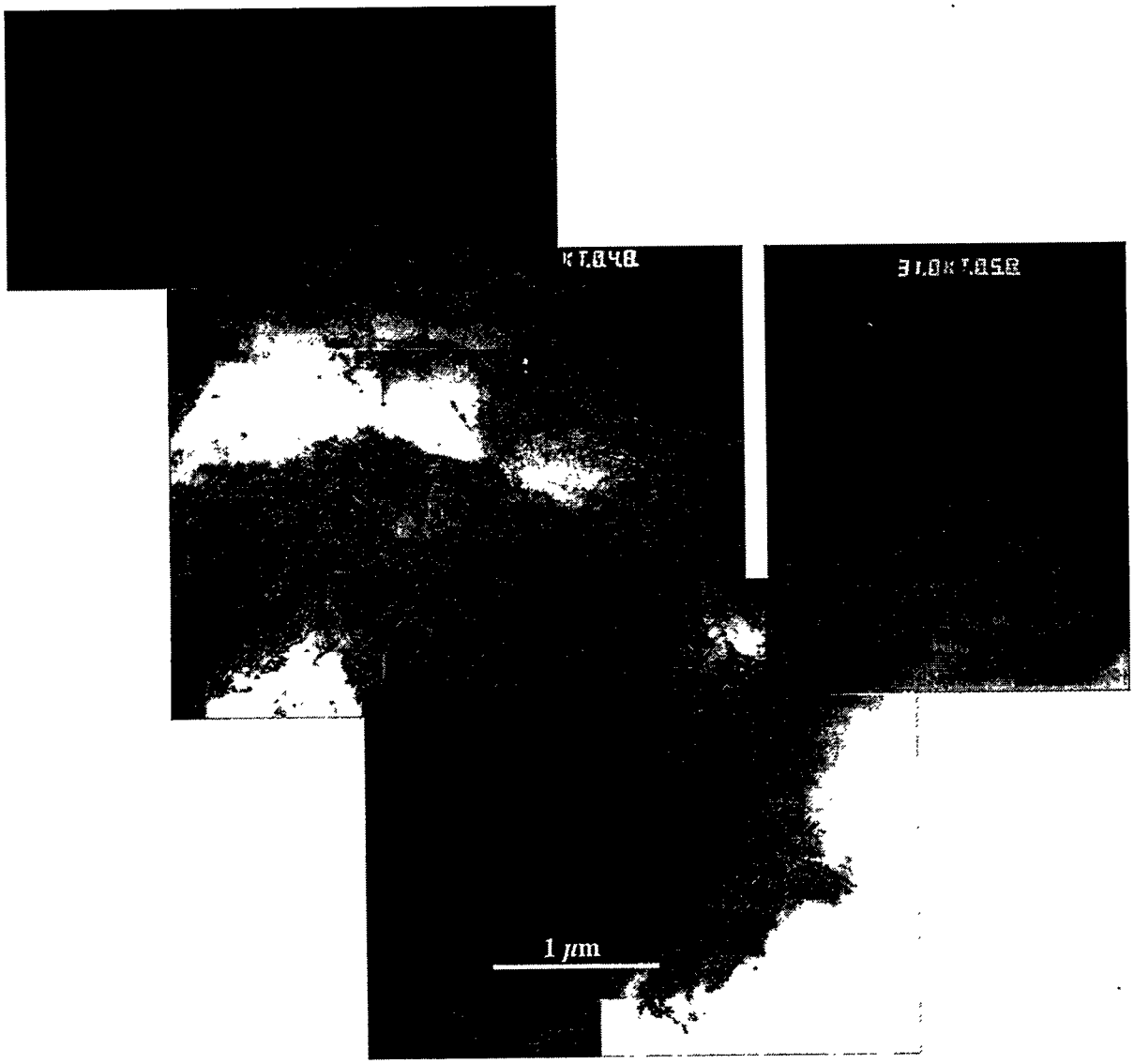

Figure 54 - Bright field TEM micrograph of Al_{GARS}-20Ti deformation processed to a true strain (η) of 12.1 and mounted in transverse section (specimen rod axis normal to the plane of the micrograph).

4.7 Phase spacing measurements and phase morphology observations

The spacing between the filaments is an important factor to determine the strength of a DMMC since the filaments act as barriers to dislocation motion. The filament spacing was calculated from SEM and TEM negatives using a circle of known diameter, and then counting the number of filaments that intercepted the circle (N_L).

In this study the mean true spacing was measured using

$$\sigma_t = \sigma_r/2 = 2/N_L$$

where N_L = number of particles intercepted per unit length of test line and σ_r = mean random spacing. Mean true distance (λ) between the particles is given by

$$\lambda = (1 - V_f)/N_L = V_m/N_L$$

where V_f is the volume fraction of fibers, V_m is the volume fraction of the matrix and N_L is the number of interceptions per unit length of test lines width he fibers. The average filament thickness (t) of the Ti fibers was estimated from the following equation:

$$t = (1 - V_m)/N_L = V_f/ N_L$$

where V_m is the volume fraction of the matrix, V_f is the volume fraction of fibers, and N_L is the number of interceptions per unit length of test lines with the fibers. Figure 55 and Table 6 shows the relation between the mean true distance and the thickness of the filaments. The filament thickness and spacing decrease with increasing deformation true strain. The values for the two highest true strain samples (η=10.3 and 12.1) were measured from TEM images while the values for the lower η samples (η=2.5 and 7.7) were measured from SEM images.

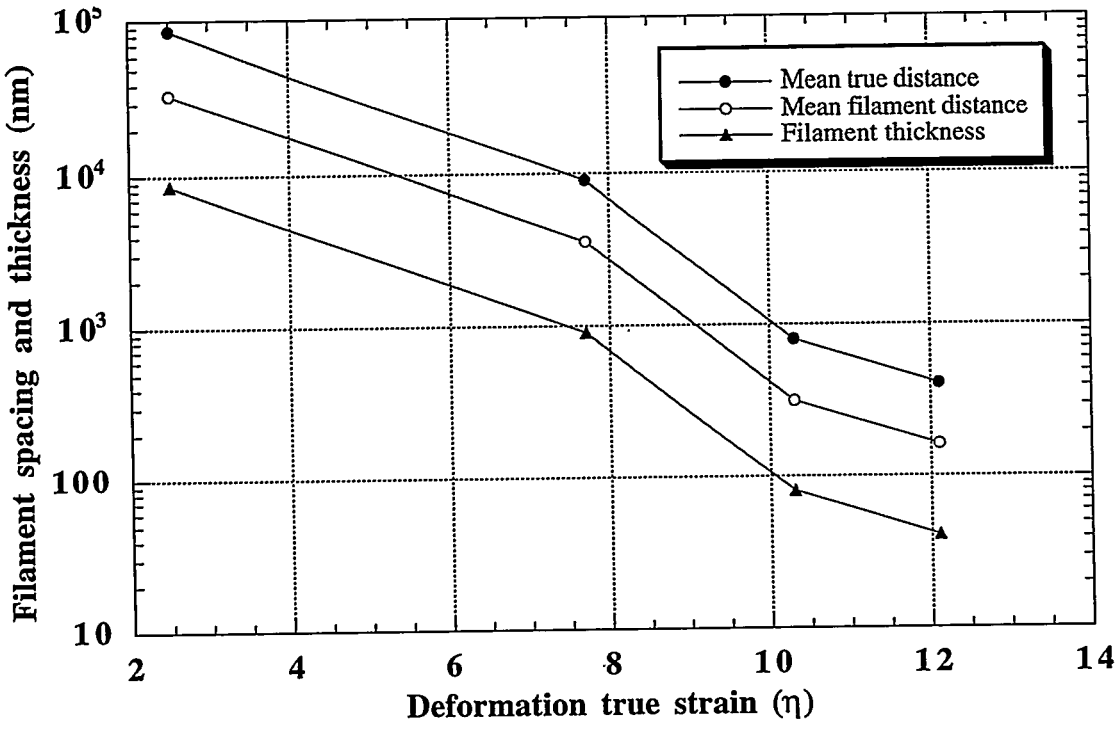

Figure 55 - Mean true spacing, mean true distance, and Ti filament thickness as a function of true strain for Al_{GARS}-20Ti.

Table 6 - Mean true spacing, mean free distance, and Ti filament thickness at various true strains for Al_{GARS}-20Ti.

True strain (η)	Mean true spacing (σ_t)	Mean free distance (λ)	Filament thickness (t)
2.5	85 676 nm	34 270 nm	8 568 nm
7.7	9 051 nm	3 621 nm	905 nm
10.3	803 nm	321 nm	80 nm
12.1	412 nm	165 nm	41 nm

Previous investigations [3] have showed that phase spacing measurements from TEM images give a smaller number than from SEM images of the same material. This is probably the reason for the change in slope between η=7.7 and η=10.3 in Figure 55 [3].

Previous investigators of DMMC's have quantified the relationship between filament spacing and ultimate tensile strength using a relation similar to the Hall-Petch-type power function for yield strength. In Cu-20Nb axisymmetrically deformed DMMC's [3,6] UTS change was proportional to (Nb filament spacing)^x where x varied between -0.5 at low strains to -0.38 at high strains, while in axisymmetrically deformed Ti-20Y DMMC [13], UTS change was proportional to (Y filament spacing)$^{-0.37}$. In the Al_{GARS}-20Ti DMMC's of this study, the relation between ultimate tensile strength and mean true spacing between Ti filaments is:

$$UTS = 2254\sigma_t^{-0.25}$$

where *UTS* = Ultimate tensile strength (MPa) and σ_t= mean true spacing of Ti filaments (nm). This shows a less strengthening than both Cu-Nb and Ti-Y. These relationships are quite sensitive to the resolution of the microscopy used to photograph the microstructure for stereology and the equipment used to obtain these micrographs (TEM vs. SEM), and comparisons between different investigations are therefore difficult to make with confidence [3]. A relationship between filament spacing and UTS measured from only SEM or only TEM micrographs would be more accurate for comparison.

Another possible reason for the lesser strengthening is that the average dendrite size of Nb in as cast Cu-Nb DMMCs is typically in the range 2-8μm, while the particle size of the titanium-powders used in this study had a maximun size of 150μm. A smaller starting powder would probably give a higher strengthening upon deformation, since strength generally increases with increasing deformation and decreasing particle size and spacing.

SUMMARY AND CONCLUSIONS

Al_{GARS}-20Ti DMMC has the advantage that it has a high ratio of ultimate tensile strength to electrical resistivity (UTS:ρ). A survey of Al alloy properties in engineering handbooks [42] shows that Al-20Ti DMMC's (η=12.1) has a UTS: ratio that exceeds any commercially available alloy.

The ultimate tensile strength of the Al_{GARS}-20Ti DMMC more than quadruples as the deformation processing proceeds from η=2.5 to η=12.1. The Ti phase changes shape from the initially equiaxed powder particles to elongated filaments with the kinked, ribbon-shaped morphology commonly observed in axisymmetrically deformed composites. The composite has a plane straining Ti-phase in a very ductile Al FCC matrix, and display a large increase in strength as the titanium phase spacing and thickness decrease. The strength of the Al_{GARS}-20Ti DMMC is due to the closely spaced Ti filaments in a pure Al matrix, and the large amount of dislocations that form during deformation.

The resistivities of Al-alloys are generally low [42]. Most of the Al-alloys have resistivities in the range 35-58 nΩ·m. The resistivity of Al_{GARS}-20Ti is good (43 nΩ·m), even though the resistivity of pure Ti is rather high for a metal (ρ=420 nΩ·m). This is because 80% of the cross sectional area of the DMMC is comprised of long strands of high-purity Al (ρ=26.5 nΩ·m at 300 K) which form a parallel conduction path with the Ti filaments.

The relation between ultimate tensile strength and mean true spacing between Ti filaments is:

$$UTS = 2254\sigma_t^{-0.25}$$

where *UTS* = Ultimate tensile strength (MPa) and σ_t= mean true spacing of Ti filaments (nm). These relationships are quite sensitive to the resolution of the equipment used to obtain these micrographs (TEM vs. SEM), and comparisons between different investigations are therefore difficult to make with confidence [3].

Although the ultimate tensile strength of 596 MPa at η=12.1 for the Al_{GARS}-20Ti is relatively high, some of the precipitation-hardened commercial Al alloys have ultimate tensile strengths of nearly 700 MPa. It remains for future studies to determine whether deformation beyond η=12.1 would further strengthen an Al_{GARS}-20Ti DMMC. A potential advantage of the Al_{GARS}-20Ti DMMC is that it may be superior to the precipitation-hardened

Al alloys in its resistance to loss of strength after exposure to elevated temperatures. Precipitation hardening alloys revert to equilibrium solid solutions at high temperature, which decreases their strength substantially. This study's 24 hours anneal at 200°C had no effect on the room temperature strength of the Al_{GARS}-20Ti DMMC, while most precipitation hardening in Al-alloys occurs at 120-190°C [48].

A longer exposure of the Al_{GARS}-20Ti DMMC to high temperature would react the two pure metals to form Al_3Ti intermetallic compound in an Al matrix. This happened in the third extrusion of the Al_{GARS}-20Ti DMMC that resulted in a two-phase Al and Al_3Ti microstructure.

It remains for future study to look at the corrosion of this alloy, although it's not expected to be significant. A mixture of Al-9wt.% Ti would also be of interest, since this composition would give an alloy of Al-20vol.% Al_3Ti during heat treatment. 20 vol.% Al_3Ti is the optimum composition for strength and ductility, and this would also be a slightly lighter and cheaper material.

REFERENCES

1. J. D. Verhoeven: *Fundamentals of Physical Metallurgy*, Wiley & Sons, New York, NY, 1975, pp. 515-519.
2. J. Bevk, J. P. Harbison, and J. L. Bell: *J. Appl. Physics*, 1978, vol. 49(12), pp. 6031-6038.
3. J. D. Verhoeven, L. S. Chumbley, F. C. Laabs, and W. A. Spitzig: *Acta Metall.*, 1991, vol. 39(11), pp. 2825-2834.
4. J. D. Verhoeven, W. A. Spitzig, L. L. Jones, H. L. Downing, C. L. Trybus, E. D. Gibson, L. S. Chumbley, L. G. Fritzmeyer, and G. D. Schnittgrund: *J. Mater. Engineering*, 1990, vol. 12(2), pp.127-139.
5. C. L. Trybus: *Microstructure-strength relationship of heavily deformed Cu-based composites*, Iowa State University, Ames, Iowa, Ph.D. dissertation, 1988.
6. W. A. Spitzig, and P. D. Krotz: *Acta Metall.*, 1988, vol. 36(7), pp. 1709-1715.
7. W. A. Spitzig, A. R. Pelton, and F. C. Laabs: *Acta Metall.*, 1987, vol. 35 (10), pp. 2427-2442.
8. J. D. Verhoeven, F. A. Schmidt, E. D. Gibson, and W. A. Spitzig: *JOM*, 1986, vol. 38(9), pp. 20-24.
9. J. D. Verhoeven, W. A. Spitzig, F. A. Schmidt, and C. L. Trybus: *Mat. & Mfg. Proc.*, 1989, vol. 4(2), pp. 197-209.
10. J. D. Verhoeven, W. A. Spitzig, F. A. Schmidt, P. D. Krotz, and E. D. Gibson: *J. of Mat. Sci.*, 1989, vol. 24, pp. 1015-1020.
11. C. L. H. Thieme, S. Pourrahimi, and S. Foner, *Scripta Met & Mat*, 1993, vol. 28, pp. 913-918.
12. A. M. Russell, L. S. Chumbley, and L.L. Keehner, 1996-1997, *unpublished research on Al-Nb and Al-Ti DMMC's.*
13. A. M. Russell: *Microstructure-strength relationships of a deformation processed titanium-yttrium composite*, Iowa State University, Ames, IA, Ph.D. dissertation, 1994.
14. A. M. Russell, T. W. Ellis, and L. S. Chumbley: *J. Mater. Sci.*, 1995, vol. 30, pp. 2070-2076.
15. A. M. Russell, L. S. Chumbley, T. W. Ellis, F. C. Laabs, B. Norris, and G. E. Donizetti: J. *Mater. Sci.*, 1995, vol. 30, pp. 4249-4262.
16. A. M. Russell, J. A. Jensen, L. S. Chumbley, D. G. Konitzer, and T. W. Ellis: *Titanium '92: Science and Technology*, ed. F. Froes and I. Caplan, TMS, Warrendale, PA, 1993, pp. 407-414.

17. J. A. Jensen, A. M. Russell, T. W. Ellis, and L. S. Chumbley: *Aluminum and Magnesium for Automotive Applications*, ed. J. D. Bryand and D. R. White, TMS, Warrendale, PA, 1996, pp. 173-187.
18. J. A. Jensen, A. M. Russell, T. W. Ellis, and L. S. Chumbley: *Light Metals 1995*, ed. J. Evans, TMS, Warrendale, PA, 1995, pp. 1367-1374.
19. J. A. Jensen: *Microstructure-strength relationships of heavily deformed magnesium-lithium composites containing steel fibers*, Iowa State University, Ames, IA, Ph.D. dissertation, 1997.
20. W. Johnson and P. B. Mellor: *Engineering Plasticity*, Van Nordstrand Reinhold, New York, NY, 1973, pp. 109-110.
21. S. W. Tsai and H. T. Hahn: *Intro. to Composite Materials*, Technomic, Lancaster, PS, 1980, pp. 381-388.
22. P. D. Funkenbusch, and T. H. Courtney: *Scripta Metall.*, 1989, vol. 23, pp. 1719-1724.
23. W. A. Spitzig, J. D. Verhoeven, C. L. Trybus, and L. S. Chumbley: *Scripta metall.*, 1990, vol. 24, pp. 1171-1174.
24. P. D. Funkenbusch, and T. H. Courtney: *Scripta Metall.*, 1989, vol. 24, pp. 1175-1180.
25. W. A. Spitzig, J. D. Verhoeven, C. L. Trybus, and L. S. Chumbley: *Scripta Metall.*, 1990, vol. 24, pp. 1181-1182.
26. P. D. Funkenbusch and T. H. Courtney: *Scripta Metall.*, 1989, vol. 24, pp. 1183-1184.
27. W. A. Spitzig: *Acta Metall.*, 1991, vol. 39(6), pp. 1085-1090.
28. G. Y. Chin: *ASM Metals Handbook*, 1985, vol. 8, 8th ed., pp. 229-232.
29. A. Pikalov, V. V. Vorob'yev, I. I. Papirov, and A. S. Kapcherin: *Izv. Akad. Nauk SSSR*, Metally, 1983, vol. 4, pp. 153-156.
30. A. R. Pelton, F. C. Laabs, W. A. Spitzig, and C. C. Cheng: *Ultramicroscopy*, 1987, vol. 22, pp. 251-266.
31. J. D. Verhoeven, W. A. Spitzig, L. L. Jones, H. L. Downing, C. L. Trybus, E. D. Gibson, L. S. Chumbley, L. G. Fritzmeyer, and G. D. Schnittgrund: *J. Mater. Engr.*, 1990, vol. 12(2), pp. 127-139.
32. Morris and Morris: *Acta. Metall.*, 1991, vol. 39(8), pp. 1763-1770.
33. W. F. Hosford, Jr.: *Trans. Met. Soc. AIME*, 1964, vol. 230, pp. 12-15.
34. G. Frommeyer and G. Wassermann: *Acta Metall.*, 1975, vol. 23, pp. 1353-1360.
35. J. D. Embury: *Scripta Metall.*, 1992, vol. 27, pp. 981-986.
36. T. W. Ellis, I. E. Anderson, H. L. Downing, and J. D. Verhoeven: *Metallurgical Transactions A*, jan. 1993, vol. 24A, pp. 21.

37. S. T. Kim, P. M. Berge, and J. D. Verhoeven: *J. Mater. Engr.*, 1995, vol.4(5), pp. 573-580.
38. T. B. Massalski, J. L. Murray, L. H. Bennett, and H. Baker: *Binary alloy phase diagrams, ASM*, Metals Park, Ohio 44073, 1986, vol. 1, pp. 173 and 175.
39. B. W. Christ: *ASM Metals Handbook*, 1985, vol. 8, pp. 28-32.
40. B. D. Cullity: *Elements of x-ray diffraction*, second edition, 1978, Addison-Wesley Pub. Co., Reading, Mass., pp. 297-321.
41. G. Y. Chin: *ASM Metals Handbook*, 1985, vol. 8, 8th ed., pp. 700-705.
42. H. Hunsicker: *"Aluminum"*, ASM Metals Handbook, 1985, edited by H.E. Boyer and T.L. Gall, ASM, Metals Park, OH, USA.
43. E. Hashimoto, Y. Ueda, H. Tamura, and T. Kino: *J. Phys Soc Jpn*, 1993, vol. 62(12) pp. 4178-4181.
44. Metals Handbook: *"Properties and Selection: Nonferrous Alloys and Pure Metals"*, 1979, vol.2, 9th edition, edited by H.Baker, ASM, Metals Park, OH, USA, p. 41.
45. B. A. Cook, J. L. Harringa, and S. Loughlin: *Mat Sci Eng*, 1996, vol. B41, pp. 280-288.
46. Tegart, W. J. McGregor: *Elements of mechanical metallurgy*, Macmillan, 1966, p. 732.
47. T. W. Ellis, S. T. Kim, and J. D. Verhoeven: *JMEPEG*, 1993, vol. 4, pp. 581-586.
48. W. F. Smith: *Structure and properties of engineering alloys*, McGraw-Hill Inc., 2nd ed., 1993, pp. 177-215.